GDF15 mediates inflammation-associated bone loss through a brain-bone axis

Dirk Elewaut

Dirk.Elewaut@UGent.be

VIB-UGent Center for Inflammation Research https://orcid.org/0000-0002-7468-974X

Renee Van der Cruyssen

VIB/Ghent University

Jan Devan

University of Zürich

irina Heggli

University of Zürich

Dominik Burri

Biozentrum, University of Basel https://orcid.org/0000-0002-8131-9309

Djoere Gaublomme

VIB-UGent Center for Inflammation Research

Ivan Josipovic

Ghent University

Emilie Dumas

VIB-UGent Center for Inflammation Research

Carolien Vlieghe

VIB-UGent Center for Inflammation Research

Maria Raimondo

University of Erlangen-Nuremberg

Pavel Zakharov

Washington University School of Medicine

Peggy Jacques

University Hospital Ghent

Sophie De Mits

University Hospital Ghent

Zuzanna Lukasik

VIB-UGent Center for Inflammation Research

Marnik Vuylsteke

Gnomixx

Thomas Renson
University of Calgary Cumming School of Medicine https://orcid.org/0000-0002-5503-000X
Lisa Schots
Ghent University Hospital
Guillaume Planckaert
VIB-UGent Center for Inflammation Research
Flore Stappers
VIB-UGent Center for Inflammation Research
Tine Decruy
VIB-UGent Center for Inflammation Research
Julie Coudenys
VIB-UGent Center for Inflammation Research
Teddy Manuello
VIB-UGent Center for Inflammation Research
Lars Vereecke
VIB-UGent Center for Inflammation Research
Ruslan Dmitriev
Ghent University https://orcid.org/0000-0002-0347-8718
Stijn Lambrecht
Ghent University Hospital
Luc Van Hoorebeke
Ghent University
Jo Lambert
University Hospital Ghent
Kodi Ravichandran
Washington University School of Medicine https://orcid.org/0000-0001-9049-1410
Andreas Ramming
University of Erlangen-Nuremberg https://orcid.org/0000-0002-7003-501X
Stefan Dudli
University of Zürich
Georg Schett
FAU Erlangen-Nuremberg https://orcid.org/0000-0001-8740-9615
Eric Gracey
VIB-UGent Center for Inflammation Research

Biological Sciences - Article

Keywords:

Posted Date: January 24th, 2024

DOI: https://doi.org/10.21203/rs.3.rs-3824212/v1

Additional Declarations: Yes there is potential Competing Interest. D.E. and S.L are inventors on patent WO2016050796A1.

GDF15 mediates inflammation-associated bone loss through a brain-bone axis

Renée Van der Cruyssen[1,2], Jan Devan[3,4], Irina Heggli[3,4], Dominik Burri[5,6], Djoere Gaublomme[1,2], Ivan Josipovic[7], Emilie Dumas[1,2], Carolien Vlieghe[1,2], Maria Gabriella Raimondo[8,9], Pavel Zakharov[10], Peggy Jacques[1,2,11], Sophie De Mits[2,11], Zuzanna Lukasik[1,2], Marnik Vuylsteke[12], Thomas Renson[2,11], Lisa Schots[2,13], Guillaume Planckaert[1,2,14], Flore Stappers[1,2], Tine Decruy[1,2], Julie Coudenys[1,2], Teddy Manuello[1,2], Lars Vereecke[1,2], Ruslan I. Dmitriev[14], Stijn Lambrecht[16], Luc Van Hoorebeke[7], Jo Lambert[2,13], Kodi Ravichandran[10,17], Andreas Ramming[8,9], Stefan Dudli[3,4], Georg Schett[8,9], Eric Gracey[1,2,#], Dirk Elewaut[1,2,11,#,*]

1. Unit for Molecular Immunology and Inflammation, VIB-UGent Center for Inflammation Research, 9000 Ghent, Belgium
2. Department of Internal Medicine, Ghent University, 9000 Ghent, Belgium
3. Center of Experimental Rheumatology, Department of Rheumatology, University Hospital Zurich, University of Zurich, 8091 Zurich, Switzerland
4. Department of Physical Medicine and Rheumatology, Balgrist University Hospital, Balgrist Campus, University of Zurich, 8008 Zurich, Switzerland
5. Computational and Systems Biology, Biozentrum University of Basel, CH-4056 Basel, Switzerland
6. Swiss Institute of Bioinformatics, CH-4056 Basel, Switzerland
7. UGCT-Department of Physics and Astronomy, Ghent University, 9000 Ghent, Belgium.
8. Department of Internal Medicine 3—Rheumatology and Immunology, Friedrich-Alexander-Universität Erlangen-Nürnberg (FAU) and Universitätsklinikum, 91054 Erlangen, Germany
9. Deutsches Zentrum Immuntherapie, Friedrich-Alexander-Universität Erlangen-Nürnberg (FAU) and Universitätsklinikum, 91054 Erlangen, Germany
10. Division of Immunobiology, Department of Pathology and Immunology, Washington University School of Medicine, St. Louis, MO 63110, USA
11. Department of Rheumatology, Ghent University Hospital, 9000 Ghent, Belgium
12. Gnomixx, 9090 Melle, Belgium

13. Department of Dermatology, Ghent University, 9000 Ghent, Belgium
14. Department of Orthopedics and Traumatology, Ghent University hospital, 9000 Ghent, Belgium
15. Tissue Engineering and Biomaterials Group, Department of Human Structure and Repair, Faculty of Medicine and Health Sciences, Ghent University, 9000 Ghent, Belgium.
16. Laboratory of Clinical Chemistry and Hematology, Ghent University Hospital, 9000 Ghent, Belgium
17. Unit for Cell Clearance in Health and Disease, VIB Center for Inflammation Research, Ghent, Belgium.

[#]are shared senior authors

*Correspondence: dirk.elewaut@ugent.be

Metabolic mediators play an important role in regulating inflammation[1]. Rheumatoid arthritis and spondyloarthritis are common inflammatory diseases of the joint, aggravated in context of obesity[2]. These patients experience systemic bone loss[3,4], which is not sufficiently controlled by disease-modifying therapeutics, despite adequate control of inflammation[5,6]. Here we report an unexpected role for GDF15 (Growth Differentiation Factor 15), a central mediator of food intake[7–10], in inflammation-associated bone loss. Serum GDF15 levels were found to be elevated in arthritis patients and inversely correlated with bone density. However, GDF15 itself does not appear to promote arthritis. Rather, GDF15 mediates trabecular bone loss through its receptor GFRAL, which is expressed exclusively in the hindbrain[7–10]. GDF15-GFRAL binding results in β-adrenergic activation of bone Marrow Adipogenic Lineage Precursors (MALPs), mesenchymal cells which are known to stimulate osteoclasts and trigger bone loss[11–14]. These data demonstrate how a metabolic mediator controls bone loss through a brain-bone axis in inflammatory diseases. These findings may lead to more specific therapeutic interventions to protect bone through targeting GDF15 or MALPs.

MAIN TEXT

Adipose tissue influences the function of the immune system. Obesity instigates and sustains low-grade inflammation, amplifies immune-mediated disorders and their associated comorbidities[1]. As such, factors regulating adipose tissue may aggravate inflammation.

Rheumatoid arthritis (RA) and spondyloarthritis (SpA) represent two prototypic immune-mediated inflammatory diseases that are often linked with obesity[2]. These disorders are defined by chronic inflammation of the joints and are strongly linked with systemic bone loss[4,15]. It has long been assumed that bone loss in the context of inflammation is directly mediated by inflammatory mediators, particularly cytokines[6]. Indeed, inflammation levels correlate with bone loss. However, patients treated with cytokine-targeting therapies can lack adequate control of bone loss, despite effective control of arthritis[5,6]. This suggests that contrary to the current dogma, inflammation and bone loss may not be directly coupled in inflammatory arthritis.

GDF15 (Growth Differentiation Factor 15) is an emerging metabolism-associated soluble protein[16]. It is broadly expressed by tissues of the body, including the placenta, prostate, colon, and liver[17]. The only known receptor for GDF15 is GFRAL (Glial derived neurotrophic factor Family Receptor α-Like), a molecule found uniquely in the hindbrain[7–10]. Through GFRAL, GDF15 causes weight loss by mediating food intake. As such, serum GDF15 levels are increased in patients with obesity or metabolic syndrome, likely representing a compensatory mechanism of the body to limit energy uptake[18]. Its serum levels were also found to be increased in infectious and inflammatory diseases. However, whether GDF15 actively contributes to the pathogenesis of inflammatory diseases is currently unknown[17].

Here, we reveal an unexpected role for GDF15 in inflammatory arthritis. We observed a marked elevation of serum GDF15 in arthritis patients, which negatively correlated with bone mineral density. We provide evidence that under steady-state conditions, elevated systemic GDF15 induces bone loss with no clinical or molecular signs of inflammation. In experimental arthritis, GDF15 plays no role in joint or extra-articular inflammation yet mediates trabecular bone loss. We thereby identified a novel brain-bone axis, by which GDF15-GFRAL triggers β-adrenergic activation of Marrow Adipogenic Lineage Precursors (MALPs) in the bone, resulting in their production of the osteoclastogenic factors, RANKL and M-CSF. These findings challenge the current dogma that bone loss in inflammatory disease is directly caused by inflammatory mediators and opens new pathways for protecting bone in the context of inflammation.

Increased GDF15 levels in arthritis associates with low bone density

We first measured systemic GDF15 in patients with inflammatory disease. We found an elevation of GDF15 in RA and SpA patients relative to healthy controls (HC) (**Fig. 1a**). SpA patients with peripheral joint arthritis had higher serum GDF15 than those with axial involvement. In addition, SpA patients with psoriasis had higher serum GDF15 levels than those without (**Extended Data Fig. 1a-b**). In an independent cohort, we observed a similar increase in GDF15 serum levels in PsA (Psoriatic Arthritis) patients (**Fig. 1b**). Next, we examined a cohort of psoriasis patients without arthritis. We observed a significant correlation between GDF15 serum levels and skin inflammation severity scores (PASI) (**Extended Data Fig. 1c**). Collectively, these data provide evidence that GDF15 levels are increased in various forms of immune-mediated inflammatory diseases.

As chronic inflammatory diseases are detrimental for bone homeostasis, we examined whether serum GDF15 levels are associated with bone mineral density (BMD) measured by dual-energy

X-ray absorptiometry (DEXA). We found a strong negative correlation between serum GDF15 and BMD in the hip and femoral regions rich in trabecular bone in RA patients, but not HC (**Fig. 1c, Extended data Fig. 1d**).

We next explored publicly available genome-wide association studies to see if the *GDF15* or *GFRAL* loci are linked to inflammatory diseases and/or BMD. We also included BMI given GDF15's role as a weight regulator. We included control genes with established pathogenic roles in inflammatory diseases, such as *TYK2*[19]. Single nucleotide polymorphisms (SNPs) at the *GDF15/GFRAL* loci were linked to BMI and/or BMD, whereas inflammatory gene SNPs were not (**Fig. 1d**). Thus, the genetic link of the GDF15-GFRAL axis with BMD strongly supports a biological role for GDF15 in bone homeostasis.

GDF15 induces dose-dependent bone loss but not tissue inflammation

To evaluate the *in vivo* function of GDF15 we first assessed the impact of GDF15 overexpression in mice. The half-life of recombinant GDF15 in the serum is short (less than 8 hours[20]), which hampers its use in long-term studies. We circumvented this by engineering an Enhanced Episomal Vector (EEV) to express murine GDF15 under the control of a CAGs promotor (**Extended data Fig. 2a**). Administering an EEV using hydrodynamic tail vein injection results in sustained protein expression[21]. GDF15-EEV was injected at different doses, after which the mice were closely monitored for seven weeks, with an extensive range of tissues studied at endpoint (**Extended Data Fig. 2b**). As a control, we used the same plasmid without the GDF15 insert (control EEV).

Serum GDF15 levels remained stable over time and dependent on the initial EEV dose, indicating a robust *in vivo* overexpression (**Extended Data Fig. 2c**). Furthermore, we observed

a dose-dependent decrease in body weight, consistent with GDF15's described role in weight control (**Fig. 2a**)[7,10]. Weight loss caused by both 1 µg and 5 µg EEV doses overlapped, suggesting receptor saturation. Therefore, we pooled these groups in further read-outs. GDF15-EEV-induced weight loss was confirmed by weighing the visceral adipose tissue depot (VAT) (**Extended Data Fig. 2d**). Together, these data demonstrate that GDF15-EEV is a robust and efficient tool to study the *in vivo* impact of chronically elevated GDF15.

As we observed serum GDF15 levels to be increased in inflammatory diseases, we initially hypothesized that GDF15 itself acts as a proinflammatory mediator. However, GDF15 overexpression did not induce clinical signs of inflammation (e.g., joint swelling, diarrhoea, skin flaking) or pain (e.g., hunched back, semi-closed eyes), with mice appearing healthy (**Extended Data Fig. 2e**). We extended this analysis using two complementary approaches. First, we evaluated intestine and joint inflammation by histopathology, but found none (**Fig. 2b, Extended Data Fig. 2f**). Next, we explored whether GDF15 could alter immune cell composition by in-depth flow cytometry of the spleen, mesenteric lymph nodes and intestine lamina propria, but found no differences in immune cell frequencies or distribution (**Extended Data Fig. 2g-h**). These data indicate that GDF15 itself does not cause inflammation, despite being associated with inflammation.

To further explore the biological activity of GDF15 we performed bulk RNAseq on an array of organs. We analysed the joint, intestine, liver (the tissue in which the EEV resides) and VAT (known to be affected by GDF15). *Gdf15* was found to be a DEG (Differentially Expressed Gene) in the liver, validating its overexpression (**Extended Data Fig. 3a**). Globally, there was no change in inflammatory genes such as *Nfkb1* and *Stat3* with GDF15 overexpression, nor liver-specific inflammation-associated transcription factors (**Extended Data Fig. 3b**). In the

liver, we found GDF15 to regulate pathways involved in lipid metabolism (**Fig. 2c**). In VAT we only found downregulated pathways, involved in angiogenesis and thermogenesis, reflecting fat deposit shrinking (**Extended Data Fig. 3c**). Contrary to the large number of DEGs in the liver and VAT, both the intestine and joint showed only a limited amount (**Extended Data Fig. 3d**), confirming the lack of pathological changes in these tissues. Collectively, these data confirm that GDF15 induces metabolic changes but show no evidence for it inducing inflammation.

Given the association between BMD and GDF15 in humans, we evaluated bone homeostasis in mice upon GDF15 overexpression. In our RNAseq dataset from the joints, we noticed a dose-dependent increase of osteoclast-associated genes, the major bone eroding cell type (**Extended Data Fig. 3e**). We therefore performed μCT (micro-computed tomography) scans of the calcaneus (heelbone) (**Fig. 2d**) and the tibia (**Extended Data Fig. 3f**) to assess peri-articular and extra-articular bone loss respectively. Interestingly, we observed a dose-dependent reduction in overall bone density and cortical and trabecular bone volume and thickness. Thus, GDF15 induces systemic bone loss independently of inflammation.

GDF15-induced bone loss is GFRAL-dependent, but independent of weight loss

GFRAL is the only known receptor for GDF15 and thus is likely the route through which GDF15 mediates bone loss. To this end, we generated GFRAL-deficient mice (**Extended Data Fig. 4a**), to which we administered GDF15-EEV (**Fig. 3a**). As anticipated, we observed a complete protection against GDF15-induced body weight and fat loss in GFRAL-KO mice (**Fig. 3b, Extended Data Fig. 4b**). Next, we assessed the bone using μCT, which showed that GFRAL-KO mice are protected against GDF15-induced trabecular but not cortical bone loss (**Fig. 3c**). We also measured bone strength using a three-point femur bending assay, confirming

that GFRAL deficiency protects against GDF15-induced weakness of the bone (**Extended Data Fig. 4c**).

Gfral expression has only been reported in the medulla of the hindbrain. Given that we observe an effect of GDF15 far from the brain, we first ruled out GFRAL expression in bone. Despite ample detection of *Gfral* in the hindbrain, we detected no *Gfral* in bone at steady-state conditions and upon GDF15 overexpression (**Extended Data Fig. 4d**). Thus, we conclude that GDF15 mediates bone loss through GFRAL, which is not present in the bone, suggesting the existence of a novel brain-bone axis.

The GDF15-GFRAL axis is responsible for both body weight and bone loss. Therefore, we investigated the possibility that the observed bone loss is a direct consequence of the reduced caloric intake and/or consequential weight loss. To this end, we performed a pair-feeding experiment. Mice were treated with either GDF15-EEV or control EEV. We weighed the amount of food consumed by the EEV-injected groups daily and fed only this amount to mice without EEV injection (**Fig. 3d**). As previously reported[7,10], GDF15-induced body weight and VAT loss was phenocopied by caloric restriction (**Fig. 3e, Extended Data Fig. 4e**). In contrast, the reduced total bone density and trabecular bone in GDF15-EEV-treated mice was not replicated in their EEV-free, pair-fed counterparts (**Fig. 3f**). Furthermore, femurs of GDF15-EEV-treated mice were weaker than their pair-fed counterparts (**Extended Data Fig. 4f**). Thus, GDF15-mediated reduced caloric intake and subsequent weight loss are not responsible for trabecular bone loss.

GDF15 is not required for steady-state and non-inflammatory bone homeostasis

As overexpression of GDF15 causes bone loss, we next questioned whether GDF15 deficiency interferes with steady-state bone homeostasis. First, we examined if GDF15 deficiency resulted in a defect in osteoclast development or function. Cultured osteoclasts from GDF15-KO mice and WT littermates showed no difference in the number of multinucleated cells nor in bone resorption (**Extended Data Fig. 5a**). Next, we performed μCT bone analysis on adult GDF15-KO and GFRAL-KO mice and saw no bone phenotype of either mouse line. Interestingly, these mice also do not show weight gain (**Extended Data Fig. 5b-d**). Together, this shows that GDF15 is not required for osteoclast generation, bone homeostasis or body weight in steady-state.

To assess whether GDF15 acts as a universal mediator of bone loss, we examined its role in ovariectomy (OVX), a model of post-menopausal osteoporosis[22]. OVX significantly increased body weight compared to sham intervention, without an effect of GDF15 deficiency (**Extended Data Fig. 5e**). Furthermore, μCT analysis showed that GDF15-KO mice are not protected against bone loss, which was confirmed functionally by femur bending assays (**Extended Data Fig. 5f-g**). Finally, serum GDF15 levels were unaffected by OVX surgery in WT mice (**Extended Data Fig. 5h**).

Considering the age-dependent increase of GDF15[23], we next examined whether GDF15 mediates age-induced bone loss. However, 15-month-old male GDF15-KO and WT littermates showed no differences in body weight nor bone homeostasis (**Extended Data Fig. 5i-j)**. Collectively, these findings indicate that GDF15 does not act as an active contributor to bone loss in non-inflammatory conditions.

The GDF15-GFRAL axis controls IL-23-induced trabecular bone loss, but not inflammation severity

We have thus far shown that GDF15 is increased in several forms of inflammatory arthritis and that GDF15 mediates bone loss but not inflammation. We therefore hypothesized that GDF15 contributes to inflammation-induced bone loss. To address this, we searched for upstream proinflammatory cytokines that could trigger GDF15 production. Potential candidates included TNF, IL-17 and IL-23, for which targeted biologicals are currently used for treating RA, SpA and psoriasis. Therefore, we measured serum GDF15 in cytokine-driven preclinical arthritis models. While we did not detect increased GDF15 in the TNF^{emARE} SpA model[24], GDF15 levels in the IL 23 EEV model[25] doubled compared to controls, mirroring the response seen in a known GDF15-inducing model, namely obesity (**Fig. 4a**). We therefore focused on the IL-23-induced inflammation model to study the potential roles of the GDF15-GFRAL axis.

IL-23 overexpression in mice leads to clinical psoriasis and arthritis (**Extended Data Fig. 6a**) and is associated with bone loss[25]. When validating this model, we observed stable overexpression of IL-23 over four weeks, during which the mice experienced weight loss and psoriasis-like symptoms (**Extended Data Fig. 6b-d**). µCT analysis showed IL-23-induced bone loss in the tibia and calcaneus (**Extended Data Fig. 6e**). We therefore reasoned that the IL-23 model is valuable for studying inflammation-induced GDF15. To this end, we injected IL-23 EEV into GDF15-KO and GFRAL-KO mice to explore whether inflammation-induced GDF15 contributes to inflammation and/or bone loss.

First, we assessed body weight. GDF15-KO and GFRAL-KO mice displayed partial protection against weight loss but had no protection against inflammation-induced VAT weight loss (**Fig. 4b, Extended Data Fig. 6f-g**). As adipocytes are known to be directly regulated by IL-17[26], we

believe that IL-23 is a stronger regulator of adiposity than GDF15. These data suggest a potential partial involvement of endogenously increased GDF15 in inflammation-induced weight loss.

Contrary to GDF15's effect on inflammation-induced weight loss, we did not observe any significant difference in clinical dermatitis, blepharitis and arthritis scores between the genotypes (**Fig. 4c-d, Extended Data Fig. 6h**). We further investigated inflammation by histopathology of the skin, gut, and joints (**Fig. 4e, Extended Data Fig. 6i**). We found immune cell infiltrates with IL-23 overexpression in all tissues, regardless of the presence or absence of GDF15 or GFRAL. Together, these data indicate that the GDF15-GFRAL axis does not impact tissue inflammation despite being induced by IL-23.

We then assessed the bone by μCT. Intriguingly, GFRAL/GDF15-KO mice were protected against IL-23-induced trabecular bone loss, but not overall or cortical bone loss (**Fig. 4d, Extended Data Fig. 7a**). We observed similar trends in the tibia (**Extended Data Fig. 7b**). Importantly, GDF15/GFRAL deficiency was found to provide protection against femur weakening, as WT bones lost significantly more strength due to IL-23 overexpression than GDF15/GFRAL-KO mice (**Extended Data Fig. 7c**).

In sum, IL-23 induces tissue inflammation independently of GDF15, but weight and bone loss are GDF15-dependent. While IL-23 induces bone loss in both the cortex and trabeculae, only trabecular bone loss was found to be mediated by GDF15. Therefore, the cell type responsible for GDF15-mediated bone loss is likely present in the bone marrow, at a trabeculae-proximal niche, rather than on the cortical bone surface.

GDF15 activates MALPs to produce RANKL and M-CSF

Next, we aimed to identify the cell in the bone that responds to GDF15 to mediate bone loss. As established above, GDF15 mediates bone loss indirectly through a brain-bone axis. Since GDF15 has recently been shown to induce β-adrenergic signaling in adipose tissue and liver via GFRAL[27] and β-adrenergic agonists are known to induce bone loss[28], we explored publicly available bone scRNAseq datasets for β-adrenergic receptor (βAR) expression[13,29–32].

Close examination of adherent bone marrow cells from 3-month-old mice revealed *Adrb2* (β_2AR) to be strongly expressed by a novel population of mesenchymal cells, Marrow Adipogenic Lineage Precursors (MALPs) and some hematopoietic cells, but not by osteoclasts nor osteoblasts[13] (**Extended data Fig. 8a**). Other subtypes of βARs were not robustly detected in this dataset. Recently, MALPs have been shown to be able to induce bone loss by stimulating osteoclasts through RANKL and M-CSF[12,14,33,34]. Thus, we hypothesized that MALPs could be activated by βARs following GDF15 upregulation.

To study the putative link between GDF15 and MALPs we investigated the "MALP gene signature", defined by Zhong et al.[12], a collection of fourteen genes that includes shared adipocyte markers, such as *Adipoq* and *Apoe*, but also specific MALP-defining genes. One of these MALP-defining genes is *Esm1,* the sole upregulated DEG in our bulk RNAseq dataset of the joint following 7 weeks of GDF15 overexpression (**Extended Data Fig. 3d**). Close examination of this dataset revealed the MALP gene signature to be upregulated in a GDF15 dose-dependent manner (**Fig. 5a**). In contrast, osteoblast and hematopoietic cell-associated genes were not upregulated by GDF15, suggesting a unique activation of MALPs (**Extended data Fig. 8b**). An additional experiment revealed MALP gene signature upregulation in the tibia already after eight days of GDF15 overexpression (**Extended data Fig. 8c**). Finally, we

documented a profound upregulation of MALP genes in ankles of mice overexpressing IL-23 (**Extended data Fig. 8d**). Thus, GDF15 regulates the MALP gene signature in the bone in a dose-dependent manner.

To date, MALPs have only been detected by scRNAseq. We therefore sought to identify MALPs by a high throughput method, specifically flow cytometry. To this end, we performed *in silico* analysis on the single-cell dataset by Zhong et al.[35] to identify candidate novel MALP cell surface markers, namely Qa2 and CD106 (*Vcam1*). Adherent cells were released from flushed tibiae and femurs by enzymatic digestion and stained for flow cytometry (**Extended data Fig. 8e**). After gating out non-MALP cells, we found a distinct population of $Qa2^{+}CD106^{+}$ cells (**Extended data Fig. 8f**). Interestingly, these cells were not observed in the non-adherent, flushed bone marrow (**Extended data Fig. 8g**). To confirm that $Qa2^{+}CD106^{+}$ cells are MALPs, we sorted them and several additional bone marrow cell populations. Only $Qa2^{+}CD106^{+}$ cells were found to express MALP genes, thus designate them MALPs (**Extended data Fig. 8h**).

We next set out to determine how MALPs respond to GDF15. We found that four weeks of GDF15 overexpression did not affect the frequency of any adherent bone cell type, including MALPs (**Extended data Fig. 8i**). In contrast, gene expression analysis showed that GDF15 overexpression specifically upregulated MALP-defining genes (**Extended data Fig. 8j**). *Adrb2* was also significantly upregulated in MALPs, suggesting increased β-adrenergic signalling to these cells. Furthermore, GDF15 overexpression strongly upregulated the expression of osteoclast-stimuli *Tnfsf11* (RANKL) and *Csf1* (M-CSF) solely in MALPs (**Fig. 5b**). Thus, GDF15 enhances the ability of MALPs to promote osteoclast differentiation, which in turn causes bone loss.

MALPs are present in human bones

To date, MALPs have only been identified in mice. We therefore sought to identify MALPs in humans. We first explored scRNAseq data from human vertebral biopsies. Of note, in this dataset there was no additional prior enrichment for mesenchymal cells, resulting in a relatively low resolution for these cell types. Notwithstanding, we found one cluster expressing most of the human orthologues of the murine MALP gene signature. Furthermore, we found this cluster to highly express *RANKL, CSF1* and *ADRB2* (**Extended Data Fig. 9a**). These data suggest that in humans, MALP-like cells exist, which we aimed to confirm using FACS.

Based on the scRNAseq, we confirmed expression of *VCAM1* (CD106) by MALPs, but not *Qa2* as this gene has no human ortholog. Thus, we decided to use CD106 and ADRB2 to identify MALPs using flow cytometry on adherent bone cells from human knee specimens. After gating out cells of known lineages, we detected a distinct population of $CD106^{+}ADBR2^{+}$ cells, which we designated as MALPs (**Extended Data Fig. 9b**). Projecting these cells onto UMAPs of non-hematopoietic cells, confirmed MALPs to be distinct from other populations in the bone (**Extended Data Fig. 9c**). To confirm $CD106^{+}ADBR2^{+}$ cells are indeed MALPs, we sorted several cell types for qPCR analysis. $CD106^{+}ADBR2^{+}$ cells specifically express common adipocyte genes *ADIPOQ* and *CEBPA* as well as MALP-defining genes *ESM1*, *SERPINA3* and *CXCL12*, but not immune-cell associated *PTPRC* (CD45) (**Fig. 5c, Extended Data Fig. 9d**). Using these complementary approaches, we conclude that MALPs are conserved across species.

GDF15 activates MALPs through adrenergic signalling

Lastly, we aimed to identify how MALPs are activated by GDF15. Given the increased expression of *Adrb2* on MALPs following GDF15 overexpression, we reasoned that adrenergic

signalling is most likely responsible. First, we performed chemical sympathectomy using 6-OHDA, which causes degeneration of the terminal ends of the peripheral adrenergic fibers[36] (**Fig. 6a**). Both GDF15 and 6-OHDA treatments independently cause weight loss, but do not interact to affect this read-out (**Fig. 6b**). This was confirmed by comparable VAT weight loss (**Extended Data Fig. 9e**). In striking contrast, 6-OHDA effectively blocked the upregulation of the MALP gene signature by GDF15, indicating that MALP activation is regulated by adrenergic stimulation (**Fig. 6c**). Genes associated with other cell types were not affected by 6-OHDA treatment (**Extended Data Fig. 9f**).

In a second approach we used propranolol, a pan- βAR antagonist (**Fig. 6d**). Propranolol alone does not affect body and VAT weights, nor does it block the effect of GDF15 on these metrics (**Fig. 6e, Extended Data Fig. 9g**). In line with our 6-OHDA results, propranolol inhibited GDF15-induced upregulation of the MALP gene signature in the bone (**Figure 6f**). Together, these data indicate that GDF15-induced MALP activation and consequential bone loss is regulated by β-adrenergic signalling.

Altogether, we uncovered a novel role for GDF15 as a mediator of inflammation-associated bone loss (**Extended Data Fig. 10**). This pathway operates through GFRAL in the hindbrain, which in turn results in β-adrenergic stimulation of trabeculae-adjacent MALPs. GDF15 increases production of RANKL and M-CSF by MALPs, which controls the differentiation and/or activation of bone-eroding osteoclasts.

Discussion

Given the intricate relationship between metabolic mediators and inflammation, we anticipated that GDF15 would directly regulate the severity of inflammation in arthritis. Much to our

surprise, our experiments revealed the opposite: GDF15 does not induce nor modify inflammation in the joints, skin or gut, but controls bone density through a novel brain-bone axis.

The crosstalk between bone and energy metabolism was first described in the early 2000's. For example, leptin was found to control bone loss through the sympathetic nervous system's control of osteoblast activity[37,38]. Here, we uncovered a unique link between bone and energy metabolism through GDF15.

Firstly, the link between bone and energy metabolism is usually studied in steady-state conditions and non-inflammatory models of osteoporosis[39]. However, bone appears to be unaffected by GDF15 under these conditions. In stark contrast, during IL-23-driven inflammation, GDF15 mediates trabecular bone loss. This different role of GDF15 in steady state conditions and during inflammation is supported by human data, whereby GDF15 negatively correlates with BMD in RA patients, but not in HCs. Notably, reduced trabecular bone is specifically associated with an increased fracture risk in arthritis patients[40], underscoring the clinical significance of the trabeculae. We speculate that the trabecular specificity of GDF15-induced bone loss reflects the proximity of the target cells to the trabeculae[13]. Thus, it appears that the effect of GDF15 on bone is "specialized" as it primarily affects trabecular bone and does not occur independently of inflammation.

Even more remarkable, GDF15 has no inherent inflammatory properties, yet its removal effectively uncouples inflammation from bone loss. A longstanding prevailing concept states that inflammation-induced bone loss occurs directly through cytokine-mediated activation of osteoclasts[6]. However, treatment of immune-mediated inflammatory diseases such as RA and

PsA by cytokine blockade does not necessarily reverse bone loss despite controlling inflammation[5,41]. Through GDF15, we provide an explanation for this paradox.

Another unexpected aspect of GDF15's role in brain-bone crosstalk is its ability to regulate weight and bone loss through different mechanisms. This was first demonstrated in our pair-feeding experiment, whereby reduced caloric intake (mimicking GDF15) does not result in the degree of bone loss caused by GDF15 overexpression. Our chemical sympathectomy and βAR-antagonist experiments confirmed this, as we found that GDF15's effect on body weight is unaffected by blocking adrenergic signalling, while it blocks the activation of the target cells in the bone.

We identified MALPs as the target cells that link the peripheral nervous system with bone. MALPs, also called "Lepr-MSC" (mesenchymal stem cell)[31], "Adipo-CAR" (CXCL12-abundant reticular)[32], "adipo-primed mesenchymal progenitors"[29] and "pre-adipocytes"[30], are non-proliferative, non-lipid laden bone marrow adipocyte precursors which have their own unique role in the bone microenvironment. RANKL production by MALPs was shown to be essential for bone homeostasis, which was confirmed by independent research groups[33,34]. Moreover, it was previously assumed that osteoblasts and mature bone marrow adipocytes were the main producers of M-CSF in the bone, however recent evidence shows that MALPs are likely the main source of M-CSF[14,33]. Finally, to the best of our knowledge, we are the first to document the existence of MALPs in human and to show that they express the βAR.

Although MALPs have irrevocably been shown to regulate bone homeostasis, our discovery that they can be regulated by β-adrenergic signalling is novel. β-adrenergic signalling is known to reduce bone mass[28], and β-blocker use in humans is associated with higher BMD[42]. Older

studies stated that osteoblasts are the target cell type for β-adrenergic signalling-induced bone loss[39]. Although we have not formally excluded osteoblasts in GDF15-induced bone loss, recent scRNAseq shows minimal βAR expression on osteoblasts[11,43]. Furthermore, *Tnfsf11*, *Csf1* and *Adrb2* expression was higher by MALPs than osteoblasts, and only MALPs had a further increase in expression of these genes following GDF15 overexpression. Importantly, MALPs and osteoblasts derive from a common progenitor and both express *Runx2,* which is considered the master transcription factor for osteoblasts[39]. scRNAseq shows that osteoblasts uniquely express *Bglap* (osteocalcin), which we used to confirm these cells in our sorting experiment. Further studies should elucidate the role of MALPs versus osteoblasts in controlling osteoclast activation.

One limitation of this study is that we have not identified the primary source of GDF15. As GDF15 mediates bone loss in inflammatory conditions, we hypothesize that it is expressed at the site of inflammation, potentially by myeloid cells as was described before[44]. Regardless of the source, GDF15 is a circulating protein that exerts its effects in the brain. Another limitation of our study is that we have not used targeted approaches to deplete MALPs. MALP-specific KO mice do currently not exist; *Adipoq*-cre conditional depletion used in previous studies targets all adipocytes, including peripheral fat and mature bone marrow adipocytes. Older studies suggested that mature bone marrow adipocytes contribute to changes in bone density[45]. Furthermore, creating MALP-specific KO mice would be very challenging as MALPs are defined by a set of genes, rather than a single gene.

In summary, we have uncovered a novel brain-bone axis that operates under inflammatory conditions. This axis uncouples inflammation from bone loss. Our study provides evidence that blockade of GDF15 could be an effective strategy to tackle inflammation-associated bone loss.

Alternatively, therapeutics from other fields of medicine could be repurposed for the same task: β-blockers, known to enhance bone density, could be used to correct inflammation-associated osteoporosis. Finally, the knowledge generated herein could be applied to other conditions with upregulated GDF15 in which bone loss is observed, such as psoriasis, cancer, and pregnancy-associated osteoporosis[46–48].

References

1. Cici, D., Corrado, A., Rotondo, C., Colia, R. & Cantatore, F. P. Adipokines and Chronic Rheumatic Diseases: from Inflammation to Bone Involvement. Clin Rev Bone Miner Metab 18, 58–71 (2020).
2. Moroni, L., Farina, N. & Dagna, L. Obesity and its role in the management of rheumatoid and psoriatic arthritis. Clin Rheumatol 39, 1039–1047 (2020).
3. FitzGerald, O. et al. Psoriatic arthritis. Nat Rev Dis Primers 7, (2021).
4. Gravallese, E. M. & Firestein, G. S. Rheumatoid Arthritis — Common Origins, Divergent Mechanisms. New England Journal of Medicine 388, 529–542 (2023).
5. Coury, F., Peyruchaud, O. & Machuca-Gayet, I. Osteoimmunology of bone loss in inflammatory rheumatic diseases. Front Immunol 10, (2019).
6. Redlich, K. & Smolen, J. S. Inflammatory bone loss: Pathogenesis and therapeutic intervention. Nat Rev Drug Discov 11, 234–250 (2012).
7. Emmerson, P. J. et al. The metabolic effects of GDF15 are mediated by the orphan receptor GFRAL. Nat Med 23, 1215–1219 (2017).
8. Hsu, J. Y. et al. Non-homeostatic body weight regulation through a brainstem-restricted receptor for GDF15. Nature 550, 255–259 (2017).
9. Yang, L. et al. GFRAL is the receptor for GDF15 and is required for the anti-obesity effects of the ligand. Nat Med 23, 1158–1166 (2017).

10. Mullican, S. E. et al. GFRAL is the receptor for GDF15 and the ligand promotes weight loss in mice and nonhuman primates. Nat Med 23, 1150–1157 (2017).
11. Zhong, L., Yao, L., Seale, P. & Qin, L. Marrow adipogenic lineage precursor: A new cellular component of marrow adipose tissue. Best Pract Res Clin Endocrinol Metab 35, (2021).
12. Yu, W. et al. Bone marrow adipogenic lineage precursors promote osteoclastogenesis in bone remodeling and pathologic bone loss. Journal of Clinical Investigation 131, (2021).
13. Zhong, L. et al. Single cell transcriptomics identifies a unique adipose lineage cell population that regulates bone marrow environment. Elife 9, (2020).
14. Zhong, L. et al. Csf1 from marrow adipogenic precursors is required for osteoclast formation and hematopoiesis in bone. Elife 12, (2023).
15. Ritchlin, C. T., Colbert, R. A. & Gladman, D. D. Psoriatic Arthritis. New England Journal of Medicine 376, 957–970 (2017).
16. Mullican, S. E. & Rangwala, S. M. Uniting GDF15 and GFRAL: Therapeutic Opportunities in Obesity and Beyond. Trends in Endocrinology and Metabolism 29, 560–570 (2018).
17. Breit, S. N., Brown, D. A., Wang, V. & Tsai, W. The GDF15-GFRAL Pathway in Health and Metabolic Disease: Friend or Foe? Annu Rev Physiol 83, 127–151 (2020).
18. Hale, C. & Véniant, M. M. Growth differentiation factor 15 as a potential therapeutic for treating obesity. Mol Metab 46, (2021).
19. Dendrou, C. A. et al. Resolving TYK2 locus genotype-To-phenotype differences in autoimmunity. Sci Transl Med 8, (2016).
20. Wang, D. et al. GDF15 promotes weight loss by enhancing energy expenditure in muscle. Nature 619, 143–150 (2023).

21. Mortier, C. et al. RORγt inhibition ameliorates IL-23 driven experimental psoriatic arthritis by predominantly modulating γδ-T cells. Rheumatology 62, 3169–3178 (2023).
22. Komori, T. Animal models for osteoporosis. Eur J Pharmacol 759, 287–294 (2015).
23. Cao, J., Venton, L., Sakata, T. & Halloran, B. P. Expression of RANKL and OPG Correlates With Age-Related Bone Loss in Male C57BL/6 Mice. Journal of Bone and Mineral Research 18, 270–277 (2003).
24. Thiran, A. et al. Sterile triggers drive joint inflammation in TNF- and IL -1β-dependent mouse arthritis models. EMBO Mol Med 15, (2023).
25. Adamopoulos, I. E. et al. IL-23 Is Critical for Induction of Arthritis, Osteoclast Formation, and Maintenance of Bone Mass. The Journal of Immunology 187, 951–959 (2011).
26. Zúñiga, L. A. et al. IL-17 Regulates Adipogenesis, Glucose Homeostasis, and Obesity. The Journal of Immunology 185, 6947–6959 (2010).
27. Sjøberg, K. A. et al. GDF15 increases insulin action in the liver and adipose tissue via a β-adrenergic receptor-mediated mechanism. Cell Metab 35, 1327–1340 (2023).
28. Sui, B. et al. Targeted inhibition of osteoclastogenesis reveals the pathogenesis and therapeutics of bone loss under sympathetic neurostress. Int J Oral Sci 14, (2022).
29. Tikhonova, A. N. et al. The bone marrow microenvironment at single-cell resolution. Nature 569, 222–228 (2019).
30. Wolock, S. L. et al. Mapping Distinct Bone Marrow Niche Populations and Their Differentiation Paths. Cell Rep 28, 302-311.e5 (2019).
31. Baryawno, N. et al. A Cellular Taxonomy of the Bone Marrow Stroma in Homeostasis and Leukemia. Cell 177, 1915-1932.e16 (2019).

526 32. Baccin, C. et al. Combined single-cell and spatial transcriptomics reveal the molecular,
527 cellular and spatial bone marrow niche organization. Nat Cell Biol 22, 38–48 (2020).
528 33. Inoue, K. et al. Bone marrow Adipoq-lineage progenitors are a major cellular source of
529 M-CSF that dominates bone marrow macrophage development, osteoclastogenesis and
530 bone mass. Elife 12, (2023).
531 34. Hu, Y. et al. RANKL from bone marrow adipose lineage cells promotes osteoclast
532 formation and bone loss. EMBO Rep 22, (2021).
533 35. Zhong, L. et al. Single cell transcriptomics identifies a unique adipose lineage cell
534 population that regulates bone marrow environment. Elife 9, (2020).
535 36. Kostrzewa, R. M. & Jacobowitz, D. M. Pharmacological Actions of 6.
536 Hydroxydopamine. (1974).
537 37. Takeda, S. et al. Leptin Regulates Bone Formation via the Sympathetic Nervous
538 System. Cell 111, 305–317 (2002).
539 38. Ducy, P. et al. Leptin Inhibits Bone Formation through a Hypothalamic Relay: A
540 Central Control of Bone Mass. Cell 100, 197–207 (2000).
541 39. Karsenty, G. & Oury, F. The central regulation of bone mass, the first link between
542 bone remodeling and energy metabolism. Journal of Clinical Endocrinology and
543 Metabolism 95, 4795–4801 (2010).
544 40. Stemmler, F. et al. Biomechanical properties of bone are impaired in patients with
545 ACPA-positive rheumatoid arthritis and associated with the occurrence of fractures.
546 Ann Rheum Dis 77, 973–980 (2018).
547 41. Chen, T. L., Chang, K. H. & Su, K. Y. Effects of Biological/Targeted Therapies on
548 Bone Mineral Density in Inflammatory Arthritis. Int J Mol Sci 23, (2022).
549 42. Lary, C. W. et al. Association of Beta Blocker Use With Bone Mineral Density in the
550 Framingham Osteoporosis Study: A Cross-Sectional Study. JBMR Plus 4, (2020).

551 43. Dolgalev, I. & Tikhonova, A. N. Connecting the Dots: Resolving the Bone Marrow
552 Niche Heterogeneity. Front Cell Dev Biol 9, (2021).
553 44. Luan, H. H. et al. GDF15 Is an Inflammation-Induced Central Mediator of Tissue
554 Tolerance. Cell 178, 1231-1244.e11 (2019).
555 45. Tratwal, J., Rojas-Sutterlin, S., Bataclan, C., Blum, S. & Naveiras, O. Bone marrow
556 adiposity and the hematopoietic niche: A historical perspective of reciprocity,
557 heterogeneity, and lineage commitment. Best Pract Res Clin Endocrinol Metab 35,
558 (2021).
559 46. Wang, W. et al. Prostate cancer promotes a vicious cycle of bone metastasis progression
560 through inducing osteocytes to secrete GDF15 that stimulates prostate cancer growth
561 and invasion. Oncogene 38, 4540–4559 (2019).
562 47. Fejzo, M. et al. GDF15 linked to maternal risk of nausea and vomiting during
563 pregnancy. Nature (2023) doi:10.1038/s41586-023-06921-9.
564 48. Hardcastle, S. A. “Pregnancy and Lactation Associated Osteoporosis”. Calcif Tissue
565 Int 110, 531–545 (2022).
566

FIGURES AND FIGURE LEGENDS

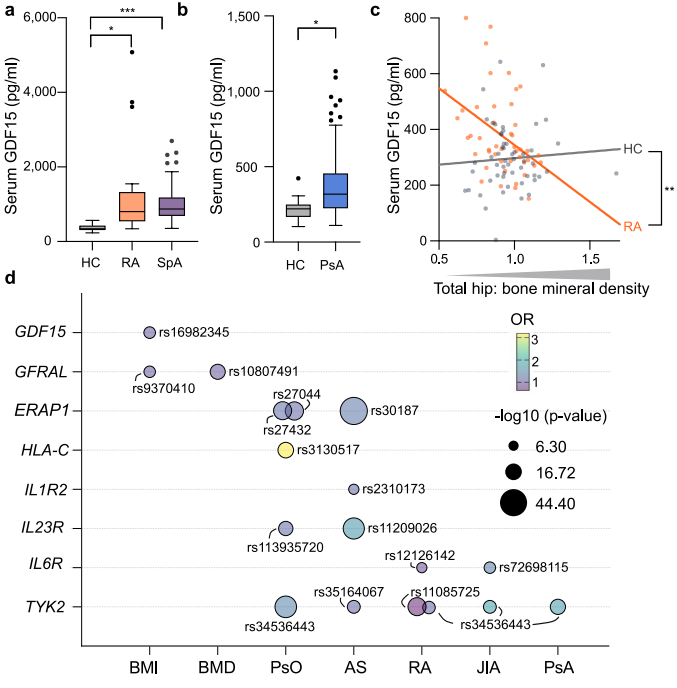
a
b
c
d
Serum GDF15 (pg/ml)
HC
RA
SpA
PsA
Total hip: bone mineral density
HC
RA
OR
-log10 (p-value)
6.30
16.72
44.40
GDF15
GFRAL
ERAP1
HLA-C
IL1R2
IL23R
IL6R
TYK2
rs16982345
rs9370410
rs10807491
rs27044
rs27432
rs30187
rs3130517
rs2310173
rs113935720
rs11209026
rs12126142
rs72698115
rs35164067
rs11085725
rs34536443
rs34536443
BMI
BMD
PsO
AS
RA
JIA
PsA

Fig. 1. Increased GDF15 levels in arthritis associates with low bone density

a, Luminex was used to measure GDF15 in serum from HC (heathy controls, n = 19), RA (Rheumatoid Arthritis, n = 20) and SpA (Spondyloarthritis, n = 111) patients. **b,** Serum GDF15 levels in an independent cohort of HC (n = 31) and PsA (Psoriatic Arthritis, n = 73) patients determined by ELISA. Tukey box and whiskers plots. One-way ANOVA was used to test for differences among patient means, followed by a post-hoc Tukey test. **c,** Serum GDF15 was measured by ELISA and bone mineral density (BMD) assessed by DEXA scan in RA patients (n = 46) and HC (n = 54). Simple linear regression with groups was used to generate regression lines between serum GDF15 and total hip BMD. The p-value refers to the significance of the difference in regression coefficients for between patient groups. Detailed information on statistics can be found in Supplementary Table 1. Each datapoint represents one patient. For all datasets, serum GDF15 concentrations were adjusted for age. Significances are indicated as: * $p < 0.05$, *** $p < 0.001$. **d,** Genome Wide Association Studies disease association analysis. Each bubble shows the lead SNP (Single Nucleotide Polymorphism) in genes of interest for the implicated phenotypes or diseases. AS = Ankylosing Spondylitis, PsO = Psoriasis, JIA = Juvenile Idiopathic Arthritis.

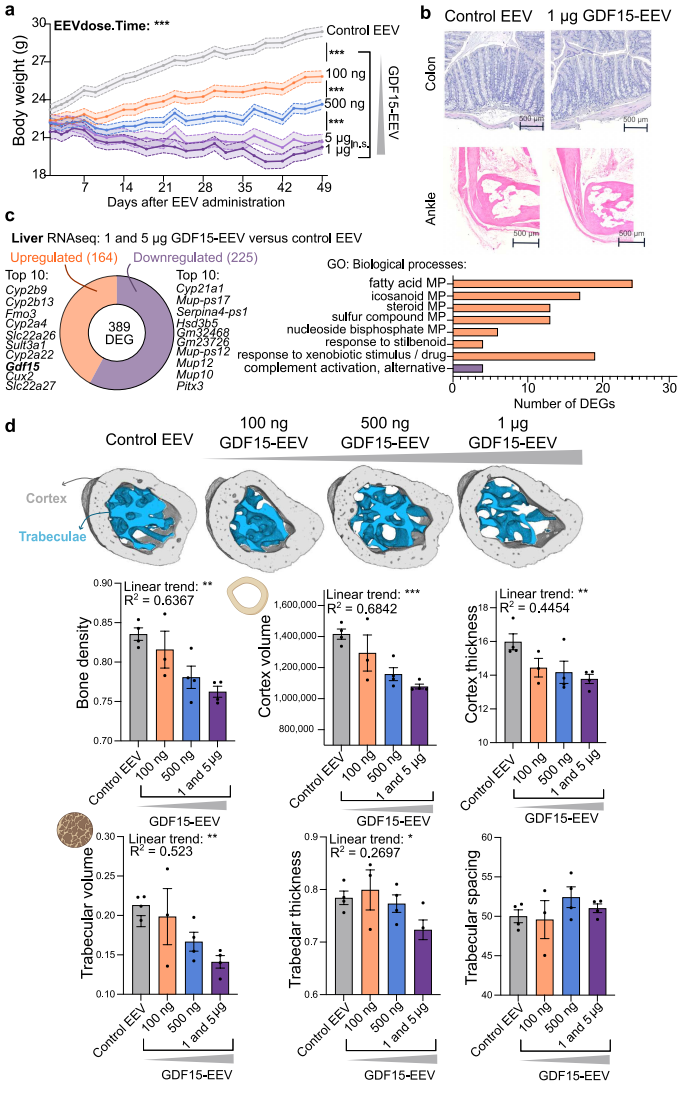
a
EEVdose.Time: ***
Body weight (g)
Days after EEV administration
Control EEV
100 ng
500 ng
5 µg
1 µg
***
n.s.
GDF15-EEV
b
Control EEV
1 µg GDF15-EEV
Colon
Ankle
500 µm
c
Liver RNAseq: 1 and 5 µg GDF15-EEV versus control EEV
Upregulated (164)
Downregulated (225)
389 DEG
Top 10:
Cyp2b9
Cyp2b13
Fmo3
Cyp2a4
Slc22a26
Sult3a1
Cyp2a22
Gdf15
Cux2
Slc22a27
Top 10:
Cyp21a1
Mup-ps17
Serpina4-ps1
Hsd3b5
Gm32468
Gm23726
Mup-ps12
Mup12
Mup10
Pitx3
GO: Biological processes:
fatty acid MP
icosanoid MP
steroid MP
sulfur compound MP
nucleoside bisphosphate MP
response to stilbenoid
response to xenobiotic stimulus / drug
complement activation, alternative
Number of DEGs
d
Control EEV
100 ng GDF15-EEV
500 ng GDF15-EEV
1 µg GDF15-EEV
Cortex
Trabeculae
Bone density
Linear trend: **
R² = 0.6367
Cortex volume
Linear trend: ***
R² = 0.6842
Cortex thickness
Linear trend: **
R² = 0.4454
Trabecular volume
Linear trend: **
R² = 0.523
Trabeclar thickness
Linear trend: *
R² = 0.2697
Trabecular spacing
Control EEV
100 ng
500 ng
1 and 5 µg
GDF15-EEV

Fig. 2. GDF15 induces dose-dependent bone loss but not tissue inflammation

a, Mouse body weight over time of mice injected with control EEV or increasing doses of GDF15-EEV (n = 2-4). Body weights were adjusted for differences in baseline body weight. A repeated measurements analysis was performed to assess overall changes in body weight over time between the four doses, represented by the EEVdose.Time interaction term, followed by testing pairwise contrasts between doses (control EEV versus 100 ng GDF15-EEV, 100 ng GDF15-EEV versus 500 ng GDF15-EEV etc.). **b,** Representative H&E-stained microscopy images of colon and ankle enthesis. **c,** Bulk RNAseq of the liver from control EEV versus 1 and 5 µg GDF15-EEV treated mice. Total number of differentially expressed genes (DEGs) (log_2 fold change > 1.0 and < 1.0, adjusted p value < 0.05), and the top 10 up- and downregulated DEGs listed. Pathway analysis using GO (Gene Ontology) terms showing the biological processes ($p < 0.001$) to which the up- or downregulated DEGs contribute. **d,** µCT of calcaneus. Representative cross-sections shown, with the bone cortex coloured in grey and trabeculae in blue. The indicated bone parameters were quantified. Bone density is bone volume divided by total volume. Trabeculae volume and thickness are normalized to the total inside volume and total bone thickness respectively. A one-way ANOVA was used to test for differences between the doses, followed by post-hoc test for trend. Results are represented as mean ± SEM, dots represent the individual mice. n.s. = not significant, ** $p < 0.01$, *** $p < 0.001$.

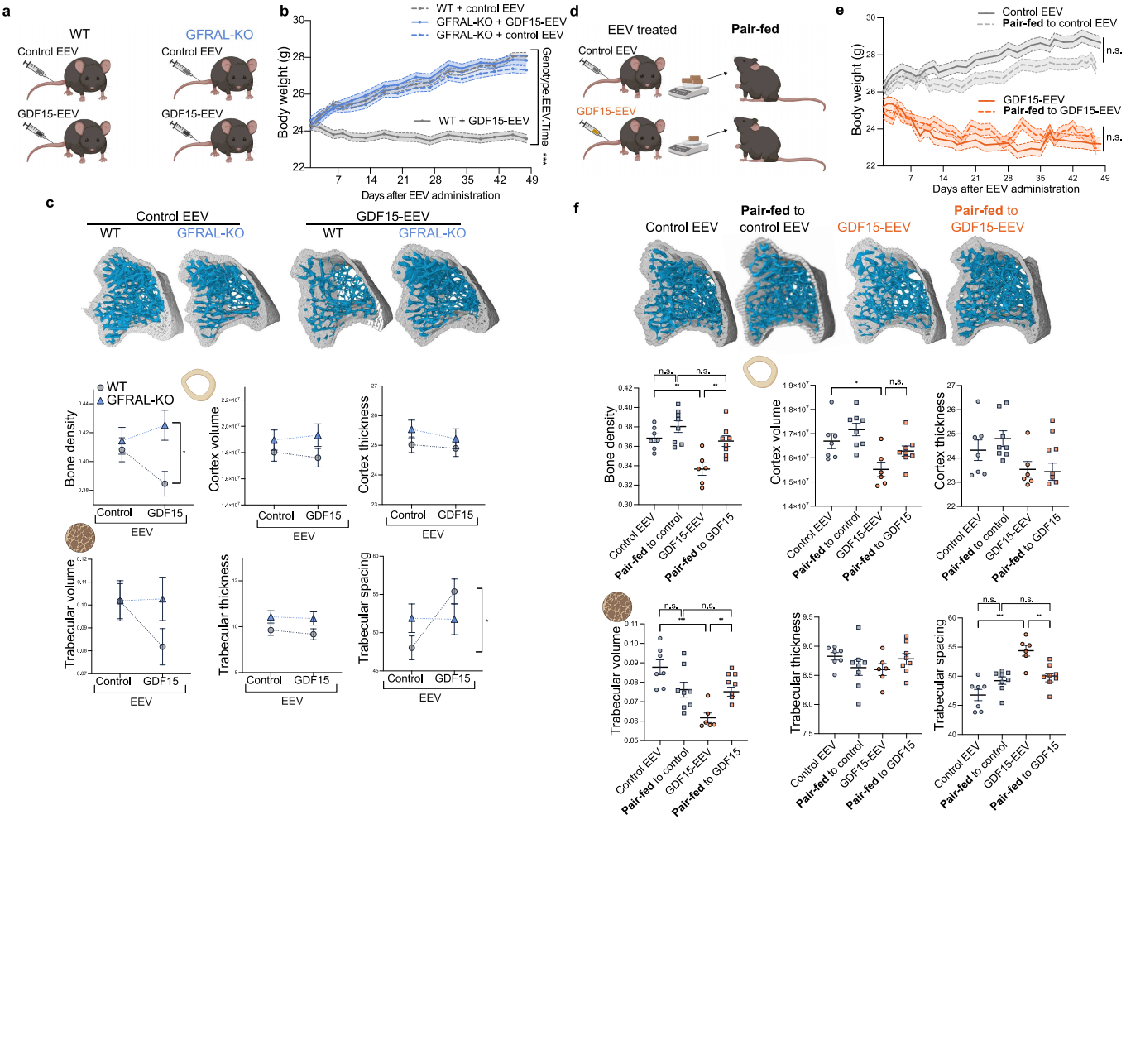
a
WT
GFRAL-KO
Control EEV
GDF15-EEV
b
WT + control EEV
GFRAL-KO + GDF15-EEV
GFRAL-KO + control EEV
WT + GDF15-EEV
Body weight (g)
Days after EEV administration
Genotype.EEV.Time
***
d
EEV treated
Pair-fed
e
Control EEV
Pair-fed to control EEV
GDF15-EEV
Pair-fed to GDF15-EEV
n.s.
c
Control EEV
GDF15-EEV
WT
GFRAL-KO
Bone density
Cortex volume
Cortex thickness
Trabecular volume
Trabecular thickness
Trabecular spacing
Control
GDF15
EEV
f
Pair-fed to control EEV
Pair-fed to GDF15-EEV
Control EEV
Pair-fed to control
GDF15-EEV
Pair-fed to GDF15
n.s.

Fig. 3. GDF15-induced bone loss is GFRAL-dependent, but independent from weight loss

a, Schematic overview of the GDF15-EEV GFRAL-KO experiment (n = 7-11). **b,** Mouse body weight over time. Statistics indicate the interaction between the Genotype (KO or WT) and EEV (GDF15 or control) over time as determined by repeated measurements analysis. Body weights are adjusted to baseline body weight. **c,** Representative μCT images of the tibia. The indicated bone parameters were quantified. A two-way ANOVA was used to test for interactions between Genotype (KO or WT) and EEV (GDF15 or control). **d,** Schematic overview of the GDF15-EEV pair-feeding experiment (n = 6-8). WT mice were treated with control EEV or GDF15-EEV and their food intake was measured daily. An equivalent amount of food was fed to non-EEV injected (pair-fed) WT mice. **e,** A repeated measurements analysis was performed to assess overall changes in body weight over time between the groups, represented by the interaction between the EEV-groups, their respective pair-fed groups and time, followed by pairwise contrast testing. Body weights were adjusted for differences in baseline body weight. **f,** Representative images of μCT of tibia. The indicated bone parameters were quantified. A one-way ANOVA was used to test for differences between the four groups, followed by post-hoc Šídák's multiple comparisons test. Results are represented as mean ± SEM. Dots represent the individual mice. Significances are indicated as: * $p < 0.05$, ** $p < 0.01$, *** $p < 0.001$.

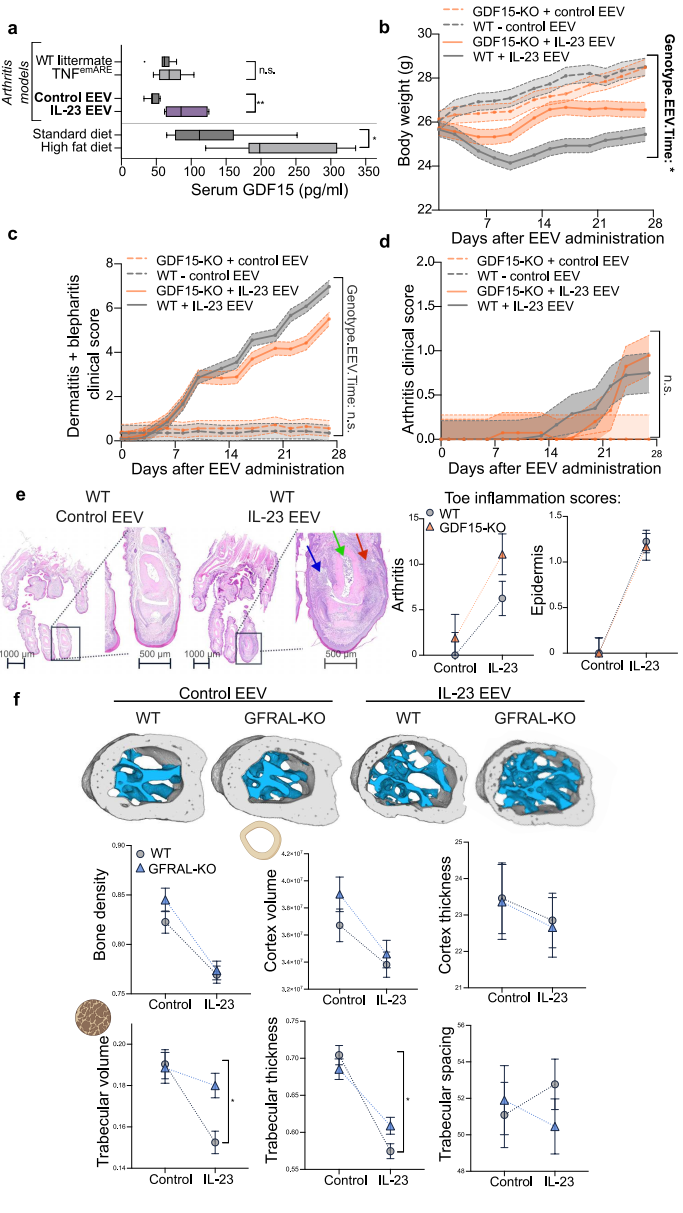
a
Arthritis models
WT littermate
TNFemARE
Control EEV
IL-23 EEV
n.s.
**
Standard diet
High fat diet
*
0 50 100 150 200 250 300 350
Serum GDF15 (pg/ml)
b
GDF15-KO + control EEV
WT - control EEV
GDF15-KO + IL-23 EEV
WT + IL-23 EEV
Body weight (g)
Genotype.EEV.Time: *
Days after EEV administration
c
Dermatitis + blepharitis clinical score
Genotype.EEV.Time: n.s.
Days after EEV administration
d
Arthritis clinical score
n.s.
Days after EEV administration
e
WT
Control EEV
WT
IL-23 EEV
1000 µm
500 µm
Toe inflammation scores:
WT
GDF15-KO
Arthritis
Epidermis
Control
IL-23
f
Control EEV
IL-23 EEV
WT
GFRAL-KO
Bone density
Cortex volume
Cortex thickness
Trabecular volume
Trabecular thickness
Trabecular spacing
Control
IL-23

Fig. 4. The GDF15-GFRAL axis controls IL-23-induced trabecular bone loss, but not inflammation severity

a, Serum GDF15 levels of C57Bl/6J mice in cytokine-driven arthritis models and obesity. An unpaired t-test was used to test the differences between disease conditions. **b,** GDF15-KO mice and WT littermates were administered either IL-23 EEV or control EEV (control EEV groups: n=5-6, IL-23 EEV groups: n=8-9) and weighed three times per week. A repeated measurements analysis was performed to assess overall changes over time between the groups, represented by the interaction between the Genotype (KO or WT), EEV (IL-23 or control) and time. Body weights were adjusted for differences in baseline body weight. **c,** Clinical scores for psoriasis-like dermatitis and blepharitis and **d,** arthritis. A repeated measurements analysis was performed to assess overall changes over time between the groups. **e,** Representative H&E-stained microscopy images and quantitative analysis of hind paw toes and distal interphalangeal joint of control EEV or IL-23 EEV-treated WT and GDF15-KO mice. Red arrow shows soft tissue infiltration, blue arrow shows joint space infiltration, green arrow shows bone marrow oedema. **f,** Representative images of μCT of the calcaneus. The indicated bone parameters were quantified. A two-way ANOVA was used to assess the interaction between genotype (KO or WT) and EEV (IL-23 or control). Results are represented as mean ± SEM. Significances of the interactions are indicated as: n.s. = not significant, * $p < 0.05$, ** $p < 0.01$.

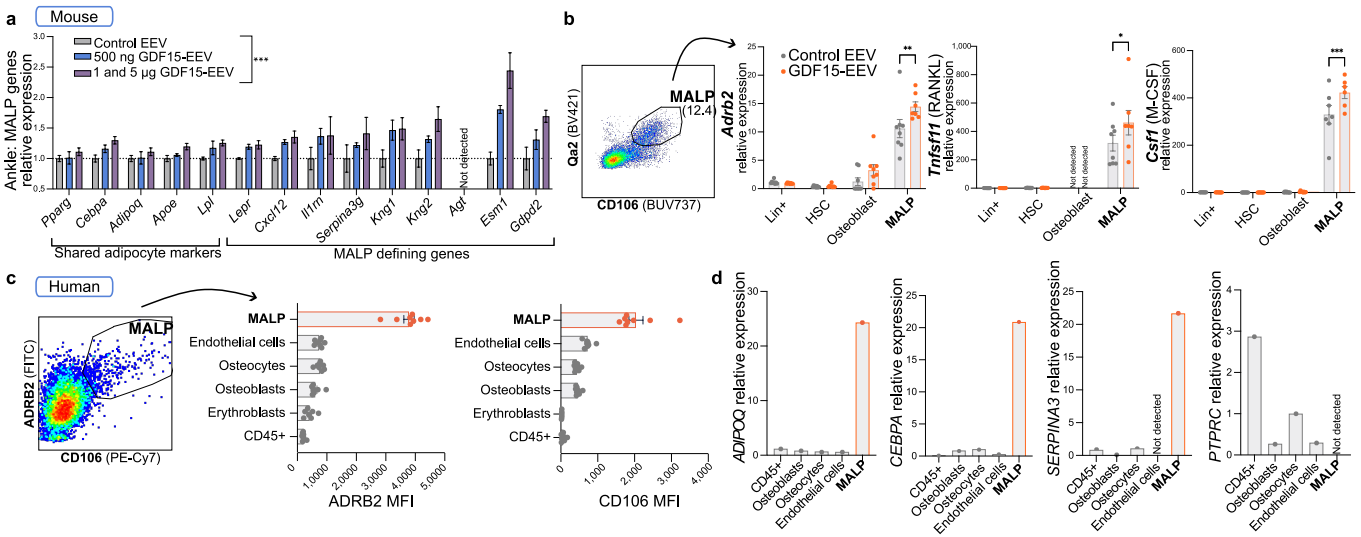
a
Mouse
Control EEV
500 ng GDF15-EEV
1 and 5 µg GDF15-EEV
***
Ankle: MALP genes relative expression
Pparg
Cebpa
Adipoq
Apoe
Lpl
Lepr
Cxcl12
Il1rn
Serpina3g
Kng1
Kng2
Agt
Not detected
Esm1
Gdpd2
Shared adipocyte markers
MALP defining genes
b
MALP
(12.4
Qa2 (BV421)
CD106 (BUV737)
Control EEV
GDF15-EEV
**
Adrb2 relative expression
Lin+
HSC
Osteoblast
MALP
Tnfsf11 (RANKL) relative expression
Not detected
*
Csf1 (M-CSF) relative expression
***
c
Human
MALP
ADRB2 (FITC)
CD106 (PE-Cy7)
Endothelial cells
Osteocytes
Osteoblasts
Erythroblasts
CD45+
ADRB2 MFI
CD106 MFI
d
ADIPOQ relative expression
CEBPA relative expression
SERPINA3 relative expression
PTPRC relative expression
Not detected

Fig. 5. GDF15 activates MALPs to produce RANKL and M-CSF and MALPs are present in human bones

a, Bulk RNAseq on the joint as discussed in Fig. 2 and Extended Data Fig. 3. Counts of each gene of the MALP (Marrow Adipogenic Lineage Precursor) gene signature is relative to control EEV. A one-way ANOVA was used to test the effect of EEV. **b,** Left, representative flow cytometry graph of MALPs in adherent bone cells (parent population: $Lin^-Sca1^-CD45^-CD31^-PDPN^-CD90^-CD34^-CD59^-$). Right, gene expression of Lin+ cells, HSCs (Hematopoietic Stem Cells), osteoblasts and MALPs of mice overexpressing GDF15 (n = 7-8). Relative expression of genes related to osteoclast stimulation (*Tnfsf11* and *Csf1*) and adrenergic receptor *Adrb2* shown. All data were normalized to reference genes *Gapdh* and *Pgk1* and are relative to expression in Lin+ cells. A two-way ANOVA was used, followed by a post-hoc Tukey's multiple comparison test. Results are represented as mean ± SEM. Significances are indicated as: *p<0.05, **p<0.01, ***p<0.001. **c,** Human MALPs were assessed using FACS on enzymatically digested human knee biopsies (n = 8). Representative flow cytometry image of human MALPs and MFI (Mean Fluorescence Intensity) of selected proteins. Each datapoint represents one patient. **d,** MALPs and other major cell populations in the bone were sorted and gene expression was determined in two pooled human samples. Expression is normalized to reference gene *GAPDH*.

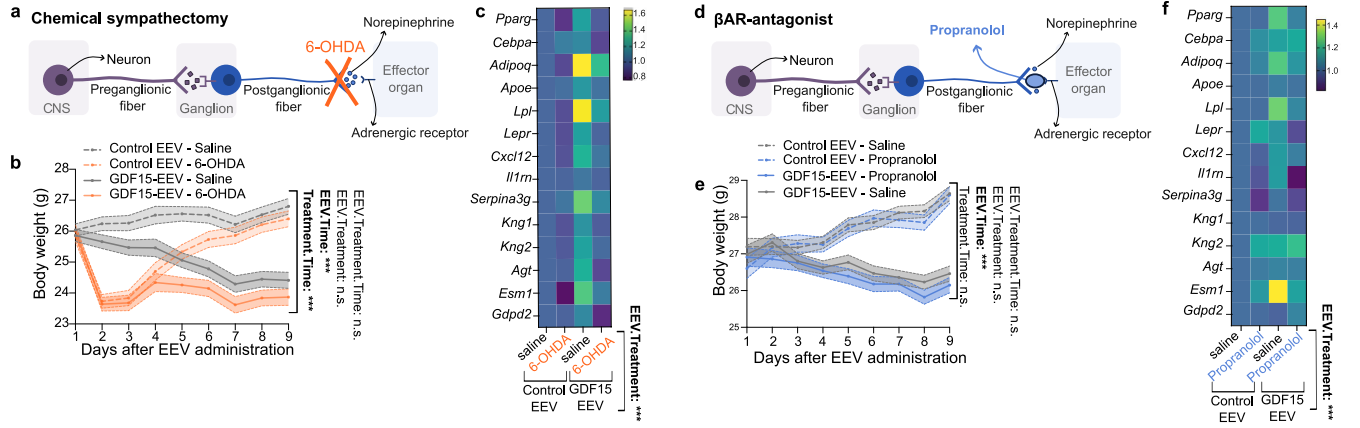
a
Chemical sympathectomy
Neuron
CNS
Preganglionic fiber
Ganglion
Postganglionic fiber
6-OHDA
Norepinephrine
Effector organ
Adrenergic receptor
b
Control EEV - Saline
Control EEV - 6-OHDA
GDF15-EEV - Saline
GDF15-EEV - 6-OHDA
Body weight (g)
Days after EEV administration
EEV.Treatment.Time: n.s.
EEV.Treatment: n.s.
EEV.Time: ***
Treatment.Time: ***
c
Pparg
Cebpa
Adipoq
Apoe
Lpl
Lepr
Cxcl12
Il1rn
Serpina3g
Kng1
Kng2
Agt
Esm1
Gdpd2
saline
6-OHDA
Control EEV
GDF15 EEV
EEV.Treatment: ***
d
βAR-antagonist
Propranolol
e
Control EEV - Propranolol
GDF15-EEV - Propranolol
f

Fig. 6. GDF15 activates MALPs through adrenergic signalling

a, Schematic of chemical sympathectomy by 6-OHDA. **b,** Mouse body weight over time of WT mice administered with GDF15-EEV or control EEV and injected with 6-OHDA or saline one day after EEV injection (n = 8-9). A repeated measurements analysis was performed to assess overall changes over time in body weight between the groups, represented by the interaction between the EEV (GDF15 or control), treatment (6-OHDA or saline) and time. Body weights were adjusted for differences in baseline body weight. Results are represented as mean ± SEM. **c,** Heatmap showing the mean gene expression of MALP gene signature in proximal tibia normalized to reference genes *Gadph* and *Pgk1* and relative to the "Control EEV – saline" treated group. A two-way ANOVA was used to assess the significance of the interaction between EEV and treatment. **d,** Schematic of the use of propranolol. **e,** Mouse body weight over time of WT mice administered with GDF15-EEV or control EEV and injected with propranolol or saline one day after EEV injection (n = 6-8). **f,** Heatmap showing the mean gene expression of MALP gene signature. n.s. = not significant, * $p < 0.05$, ** $p < 0.01$ ***$p < 0.001$.

METHODS

Patients

All patients fulfilled the ACR-EULAR for RA, the ASAS classification for SpA and CASPAR criteria for PsA. Psoriasis patients were diagnosed by an expert dermatologist. RA, SpA and psoriasis patients were diagnosed at the Ghent University Hospital, Belgium; PsA patients at Erlangen, Germany. Patient characteristics are shown in Supplementary Table 2. Vertebral bone biopsies were acquired from unaffected lumbar vertebrae from four chronic low backpain patients (mean ± SD age of 56.8 ± 10.2) undergoing spinal fusion surgery at the Balgrist University Hospital, Switzerland. Human knee samples (four femur condyle and three tibia plateau) were acquired from osteoarthritis patients (mean ± SD age of 61 ± 9.4) receiving knee-replacement surgery. Ethical approvals were obtained from the local ethics commissions and all patients gave informed consent.

Mice

C57Bl/6J mice were purchased from Janvier Labs (France). GDF15-KO mice were acquired from EUCOMM, as described in Maschalidi *et al.,* Nature (2022)[49]. GFRAL-KO mice (official name: Gfral^{em1Irc} mice, MGI ID: 7526694) were created using the CRISPR/Cas9 system (see supplementary methods). All experiments started at 10-12 weeks old and were performed in conventional housing conditions with group housing in a 12-hr light / 12-hr dark cycle and had *ad libitum* access to food and water, except when pair-fed. Male mice were used unless otherwise indicated. All experiments were approved by the Animal Ethics Committee of the Faculty of Medicine and Health Sciences, Ghent University.

Serum protein analysis

Serum GDF15 in cohort 1 was determined by an optimized Luminex Bio-Plex immunoassay at the UMC Utrecht Luminex Core Facility (University Medical Center, Utrecht, The Netherlands)[50]. GDF15 levels in the other cohorts and the mouse experiments were determined using human (R&D, Cat. DY957) or mouse ELISA (R&D, Cat. DY6385) respectively, replacing 0.1% casein in PBS by reagent diluent and avidin-HRP (Invitrogen, Cat. 18-4100-51). IL-23 levels were determined using BioLegend mouse IL-23 ELISA kit (Cat. 433704).

Public SNP data

The GWAS data was obtained using "gwasrapidd" R package[51]. First, variants for the selected list of genes were acquired using get_variants() function. Then, selected variants within 1Mb of the gene body and filtered variants related to genes outside of the original geneset were used. Function get_associations() was used to get association IDs, p-values, and odds ratio (or_per_copy_number) for every variant, then get_traits() function to extract biological traits. The R software version was 4.2.2 and "gwasrapidd" package version was 0.99.14. For the phenotypes, SNP rs10807491 is specifically associated with heel BMD.

EEV production

Mouse *Gdf15* transcript sequence was obtained from NCBI (NM_011819). The protein coding exons were flanked *in silico* by the multiple cloning site (MCS) + 10 adjacent base pairs from the CAGs-MCS EEV (Systems Bio, Cat. EEV600A-1). The *Gdf15* sequence was generated at VIB synthetic DNA core facility. To linearize the EEV, NotI (NEB, Cat. R189S) and BsrGI (NEB, Cat. R3575S) restriction enzymes were used. *Gdf15* was inserted into the linearized vector using Gibson assembly (NEB, Cat. E5520S). Next, the EEV was transformed into Stbl2 competent cells by heat shock following the manufacturer's instructions (ThermoFisher, Cat. 10268019). After serial dilution in SOC media with ampicillin, colonies were grown on agar

plates (37°C). Colonies were picked the next morning, and the culture was expanded in 100ml Luria broth with overnight shaking (200 rpm, 37 °C). EEV was extracted by endotoxin-free maxiprep (Qiagen EndoFree Maxi Kit, Cat. 12362). Colonies containing *Gdf15* inserts were sent for Sanger sequencing (Eurofins) to ensure the correct sequence was inserted. A single GDF15-EEV was selected to use for *in vivo* experiments. The IL-23 EEV was a gift from R. Inman (University of Toronto).

EEV injection and scoring

EEV was administered by HDD, in which a volume of 10 % of the mouse's body weight is injected by tail vein in less than 10 seconds. Mice were administered 1 μg GDF15-EEV, unless otherwise indicated, or 30 ng IL-23 EEV; with an equal amount of control EEV. Mice were excluded based on failed injections (e.g., insufficient volume or too slow) and/or low serum protein levels as determined by ELISA. For IL-23 EEV, mouse body weight and clinical score was assessed by two blinded investigators: arthritis (0-3), blepharitis (0-2), snout, ear and tail dermatitis (0-2 each), and paw dermatitis (0-4). Mice were sacrificed four weeks after IL-23 EEV injection or 7 weeks GDF15-EEV injection unless otherwise indicated.

OVX surgery

GDF15-KO and WT mice were anesthetized using ketamine (100 mg/kg body weight) and xylazine (16 mg/kg body weight). Both ovaries were removed, and the skin was closed using resorbing thread. Buprenorphine was administered as analgesia (0.1 mg/kg body weight). Ovary removal was confirmed using histology on the removed tissue. The mice were euthanized six weeks after surgery.

Pair-feeding experiment

EEV-groups received EEV injections on day 0 and starting from day 1 food intake and body weight were monitored daily. The mean amount of food consumed by the EEV group was given to the corresponding pair-fed mice in the afternoon. We found that the GDF15-EEV mice were pulverizing food without eating it, thereby affecting the accuracy of food intake measurements and pair-fed mice body weight. This behaviour could be a consequence of stress induced by single housing conditions combined with GDF15 overexpression. Moving forward, any EEV-treated mice displaying signs of food destruction were excluded from the measurement of mean food consumption and efforts were made to enhance the enrichment within all cages to alleviate stress levels. As a result of these observations and adjustments, body weight measurements taken between days 6 and 10 post-EEV injection for the pair-fed to GDF15-EEV mice were omitted from the statistical analysis.

6-OHDA experiment

The mice received a single intraperitoneal injection with 200 mg/kg 6-OHDA (Sigma, Cat. H4381) dissolved in saline with 0.1% ascorbic acid (Sigma, Cat. A34403) or vehicle one day after GDF15- or control EEV injection. The 6-OHDA solution was kept on ice and injected within 30 min of dissolving, to avoid breakdown of the product, observable by a colour change of the solution which did not occur. Mice were weighed daily and sacrificed on day 9. Longer experiments were not performed as 6-OHDA injury is reversible after approximately two weeks[52].

Propranolol experiment

From one day after GDF15- of control EEV injection onwards, mice received daily intraperitoneal injections with 10 mg/kg propranolol (Sigma, Cat. P0884) or saline. Body weight was measured daily. It's noteworthy to mention that some unexpected deaths occurred

among the GDF15-EEV + propranolol mice for unknown reasons. Consequently, these mice were excluded from the subsequent analysis. For this reason, we have not performed long-term propranolol treatment. The remaining mice were euthanized on day 9.

Histopathology

Upon dissection, tissues were fixed in 4 % formaldehyde overnight or 48 hours for calcified tissues (ankle, foot). These were decalcified using 5 % formic acid for five days. After dehydration, samples were paraffinized and cut at a thickness of 5 µm. Samples were stained using haematoxylin and eosin. Two blinded investigators assessed the inflammation severity in using the previously reported scoring systems[53]. For ear, skin was assessed: epidermis (0-3), based on the number of layers of keratinocytes, and dermis (0 to 4), considering thickness and the extent of immune cell infiltration. Colon scoring was based on severity (0 to 3) and extent (0 to 3) of infiltration and epithelial changes: crypt elongation (0-3) and goblet cell loss (0-3). Ankle samples were scored for Achilles tendonitis (0-2), calcaneus bone marrow oedema (0-2), infiltrate in the synovial-Achilles enthesial complex (0-2), talus-tibia-calcaneus region (0-2) and assessing the areas around the cuboidal joints: synovium (0-2), fat pad (0-2), and joint space (0-2). Toes (hind foot): For each joint, periarticular inflammation (0-3) and joint space infiltration (0-2) was assessed. For each toe, overall bone marrow oedema was scored (0-3). For each foot, epidermis thickness was evaluated at the base of the toes (0-3).

µCT

The scans were performed at the Centre for X-ray Tomography of the Ghent University (UGCT, www.ugct.ugent.be) using the HECTOR micro-CT scanner[54]. 3D reconstruction was performed using Octopus, a reconstruction software package developed at UGCT[55], yielding a 10.6 gigavoxel reconstructed volume with an isotropic voxel size of 4 µm. For details see

supplementary methods. Quantification was performed as described in Gilis *et al.*, Arthritis Rheumatology (2019)[56] and Cambré *et al*., Nature Communications (2018)[57] using an algorithm similar as in Buie *et al*.[58]. Briefly, an in-house developed script was used in ImageJ, bone structures were automatically classified into cortex and trabeculae. Both average thickness and entire volume of these structures were quantified. "Bone density" is the ratio of the "bone volume" over the "total volume". "Trabecular spacing" is the average thickness of the non-bone volume between the trabeculae. "Trabecular volume" was normalized by dividing by the "inside volume", which is calculated by subtracting the "cortical volume" (including cortical pores) from the "total volume". In calcaneus, "trabecular thickness" was normalized to "total bone thickness".

Femur bending assay

Femurs, stripped from surrounding tissue, were wrapped in a PBS-soaked gauze to prevent dehydration and stored at -20°C up until analysis. The three-point femur bending test was performed using the LRXplus (Lloyd Instruments, USA) universal testing machine located at the Department of Human Structure and Repair, Ghent University. A loading point is strategically positioned on the mid-diaphysis of the femur and is gradually moved downward, applying increasing force and displacement. The resulting maximum force (load cell 100 N) signifies the load applied immediately before the femur fractures.

***In vitro* osteoclastogenesis**

Flushed bone marrow cells from mouse femurs and tibiae were cultured in α-minimum essential medium (α-MEM) supplemented with 10 % foetal calf serum, 10 units/ml penicillin, 10 mg/ml streptomycin, 2 mM glutaMAX and 30 ng/ml M-CSF (obtained from VIB protein core facility). After overnight incubation, the non-adherent fraction was seeded at 10^6 cells/well in 24-well

plates or bone resorption plates (Bio-Connect, Cat. CSR-BRA-24) in medium containing 30 ng/ml M-CSF and 10 ng/ml RANKL (R&D Systems, Cat. 452-TEC-019). The supplemented medium was replaced after 48 hr. At day 4, TRAP staining was performed (Sigma-Aldrich, Cat. 386A-1KT). Cell numbers were determined using ImageJ.

RNA isolation

Tissues were collected in RNA Protect (Qiagen, Cat. 76106). Sorted cell pellets were lysed using RLT buffer (mouse) or QIAZol (human) (Qiagen, Cat. 79306). RNA was extracted by mixing of the tissue in TRIZol (Life Technologies, Cat. 15596-026) followed by the Qiagen RNeasy micro kit (Cat. 74004) for both tissues and cells according to the manufacturer's instructions. For VAT, an extra centrifuge step (10min, 4°C, full speed) was added after tissue mixing, to eliminate the resulting top fatty layer. For tibia, the proximal 1/3rd of the cleaned bone was used.

Mouse bulk RNAseq

RNA concentration and purity were determined spectrophotometrically using the Nanodrop ND-8000 (Nanodrop Technologies) and RNA integrity was assessed using a Fragment Analyzer (Agilent). Samples sequenced on Illumina NovaSeq 6000 (v1 kit, 100 cycles, Single Reads) at the VIB Nucleomics Core (www.nucleomics.be). For details see supplementary methods. Data is submitted at NCBI GEO (GSE248918).

Data processing

The quality of raw sequencing reads was evaluated using fastQC v0.11.9. Untrimmed reads were aligned to the mouse reference genome GRCm38 utilizing HISAT2 v2.2.0[59]. The read counts were generated using featureCounts v2.0.0[60]. For each individual subset, differential

846 expression analysis was performed using DESeq2 v1.32.0[61] in R v4.1.0. Filtering was lenient,
847 excluding genes with fewer than 10 counts. The DESeq() function, utilizing default parameters,
848 was employed for read count normalization, dispersion estimation, and linear model fitting.
849 Principal component analysis was utilized to identify potential batch effects and outliers. This
850 led us to identify one outlier in subset VAT and in ankle. To mitigate the impact of lowly
851 expressed genes and high variability, we applied the apeglm shrinkage estimator to the log fold
852 changes[62]. Significance levels were adjusted for multiple testing using the Benjamini-Hochberg
853 (BH) method. Genes were considered differentially expressed if they passed the commonly
854 used thresholds of an adjusted p-value <0.05 and an absolute log2 fold change >1.
855
856 *Pathway analysis*
857 To identify enriched Gene-Ontology biological processes, overrepresentation analysis was
858 carried out by enrichGO, a function of the R package clusterProfiler v4.0.5[63]. Prior to the
859 analysis, gene symbols were converted to Entrez ID's in R using AnnotationDbi v1.51.1 and
860 the annotation package org.Mm.eg.db v3.13.0. A custom background gene list was provided
861 containing all genes of the filtered count matrix. The analysis was performed on up- and
862 downregulated genes separately, adjusting the p-values of the enrichment result for multiple
863 testing with the BH method. GO-terms with an adjusted p-value < 0.05 were considered
864 significantly enriched.
865
866 **Human single cell RNAseq**
867 Vertebral biopsies were digested for 40min at 37°C in digestion solution (0.05% Collagenase
868 P (Sigma-Aldrich), 100µg/ml Liberase (Sigma-Aldrich), 100µg/ml DNAse I (Sigma-Aldrich)
869 in HBSS, gently flushed with digestion solution, digested for another 20min at 37°C, and
870 filtered through a 70µM filter. Red blood cells were lysed with ACK lysis buffer. Cell viability

had to be > 70% in order to proceed. Cells positive for CD45 and CD66b (Biolegend) and Zombie Aqua (Biolegend) (dead cells) were removed by FACS (FACSAria™ Fusion, BD).

Sequencing was performed on an Illumina sequencing platform (Novaseq 6000) using paired-end 28+90bp sequencing. One end of the sequencing read generated cell-specific, barcoded sequences and unique molecular identifier (UMI), while the other end captured the sequence of the expressed poly-A tailed mRNA. The sequencing was carried out using two full FP flow cells to achieve an approximate read count of 50,000 per cell. For details, see supplementary methods.

Preprocessing, quality control, and normalization*:* First, barcodes were processed, genes were aligned to the human genome (Homo_sapiens/GENCODE/GRCh38.p13/Annotation/Release_42-2023-01-30), and a count matrix was generated using the CellRanger toolkit (10x Genomics, version 4.0). Analyses were performed in R studio (version 4.2.2). Quality of cells was controlled and cells with mitochondrial content <50% and >500 counts per cell were retained (*scater,* version 1.26.1). Genes with 0 counts across all cells were removed. Data was normalized with sample as batch factor (*batchelor,* version 1.14.1).

Dimensionality reduction, clustering, integration*:* The top 57% highly variable genes (HVG) were identified (*scran,* version 1.26.2). Data was integrated on these HVGs, with number of nearest neighbours 30, and without cosine normalization with fastMNN function (batchelor*, version 1.14.1*). Clustering was performed on the corrected low-dimensional coordinates by building a shared-nearest-neighbour graph with 30 neighbours and "rank" weighting scheme (*scran*, *version 1.26.2*) and cluster detection with the Leiden algorithm using resolution of 0.75

(*igraph,* version 1.5.1). Grouped heatmaps were created with plotGroupHeatmap, with center and scale, but without clustering rows or columns (scater, version 1.26.1).

qPCR protocol and analysis

After nanodrop measurement to determine concentration and quality of RNA, cDNA was synthesized with the QuantiTect Reverse Transcription kit (Qiagen, Cat. 205314). Gene expression was determined using SYBR Green (GC biotech, Cat. QT650-05) or Fast Advanced Master Mix (Taqman, Thermofisher). Analysis was performed using qbase+ (CellCarta). All the primer sequences used can be found in Supplementary Table 3. The primers for *Bglap* cross-react with *Bglap2* and *Bglap3*, as *Bglap*-specific primers were not possible to design, but all paralogues are specifically expressed by osteoblasts.

Flow cytometry

Myeloid and lymphoid panels on spleen, MLN and gut

Spleen and the proximal three mesenteric lymph nodes (MLN) were mashed with a plunger and filtered through 70 µm. Red blood cells in spleen were eliminated using ACK (Westburg, Cat. 10-548E). For ileum and colon, lamina propria was isolated. Briefly, samples were cleaned, cut longitudinally and into 1 cm segments. While in 10ml cold HBSS, the tissues were shaken vigorously to remove any debris, after which it was filtered through nylon. Next, 10 ml of 2 mM EDTA/HBSS was added and incubated with magnetic stirring at 37 °C for 15 min at 250 rpm. After washing, this process was repeated. Finally, the intestine was minced with scissors. Samples were incubated in enzyme cocktail: 0.425 mg/ml Collagenase V (Sigma, Cat. C9263), 0.6 mg/ml Collagenase VIII (Sigma, Cat. C2139-1G), 0.75 mg/ml Collagenase D (Roche, Cat. 11088882001), and 50 µg/ml DNase (Sigma, 1128492001) 30 min with magnetic stirring at 37 °C, and the filtered through a 100µm cell strainer. Staining mixes are described in

Supplementary Table 4. Cells were fixed using the eBioscience TF fixative (Cat. 00-5523-00) according to the manufacturer's instructions and measured on a Fortessa (BD Biosciences).

Mouse MALP FACS

We performed *in silico* analysis of scRNAseq-identified, MALP-specific genes[11] to identify cell surface proteins using DAVID (Database for Annotation, Visualization and Integrated Discovery; https://david.ncifcrf.gov/). Candidate antibodies were screened in a panel to assess their expression on different cell populations and the remaining MALP-containing cells (as described below). Only Qa2 and CD106 (VCAM1) double-stained the remaining cells and were further explored as MALP markers for flow cytometry.

To isolate adherent bone marrow cells, we adapted previously published protocols[64,65]. In brief, flushed femur and tibiae longitudinally and transversally cut bone pieces were digested in PBS supplemented with 1 mg/ml collagenase I (Thermofisher, Cat. 17018029), and 0.1 mg/ml DNase I (Sigma, Cat. 11284932001) for 1 hr at 37 °C while magnetically stirring. After filtering through a 100 µm strainer, red blood cells were eliminated using ACK. The cells were stained according to Supplementary Table 4 and sorted on a Symphony S6 (BD Biosciences).

As MALPs proved to be relatively rare cells (~8000 in a total of 10 x 10^6 adherent bone cells per mouse), long sorting durations were required for each sample, making sorting of cells impractical for the large, GDF15-EEV experiment. Therefore, here we enriched for MALPs by using the BioLegend MojoSort Mouse Hematopoietic Progenitor Cell Isolation Kit (Cat. 480004) according to the manufacturer's instructions. As the MojoSort antibodies and FITC antibodies (dump channel for lineage positive cells) of our panel bind to the same antigens, staining of these antibodies was performed simultaneously. Using qPCR and FACS we ensured

946 that the positively selected (lineage positive) cells did not contain Qa2+CD106+ MALPs. Here,
947 we sorted ~10^6 negatively selected cells in which the MALP frequency was increased 10-fold.
948
949 *Human MALP FACS*
950 Human knee samples were obtained as pieces of bone removed during total knee replacement
951 surgeries and smaller pieces of trabecular bone were further removed by 4mm punch biopsy
952 tools (CLS-med). Biopsies were digested for 45-60 min at 37 °C in a digestion medium
953 containing 5 ml of HBSS (Sigma, Cat. H6638), 2.5 mg of Collagenase P (Sigma, Cat.
954 11213857001), 500 µg DNAse I (Sigma, Cat. 11284932001), and 500 µg Liberase (Sigma, Cat.
955 5401020001). After digestion, cells were flushed from the bone tissue. Single-cell suspensions
956 were cryopreserved up until FACS staining, which is described in Supplementary Table 4. For
957 sorting, we pooled single cell suspension derived from two donors prior to obtain sufficient cell
958 numbers. We first performed MACS negative enrichment using BioLegend MojoSort Human
959 anti-PE nanobeads (Cat. 480092) to sort the ADRB2^{high}CD106^{+} MALPs. Other analysed
960 populations were sorted without previous enrichment. BD FACSAria™ was used for the
961 sorting.
962
963 **Statistical analysis**
964 Statistical analyses were conducted using GraphPad Prism 9 and GenStat 22. Residual plots
965 were used to assess normal distribution of the residuals and to identify outliers.
966
967 All patient data was corrected for age. Patients using metformin were outliers as reported
968 before[66] and excluded from the GDF15 serum analysis. Simple linear regression with groups
969 was used to test for parallelism: The first model to be fitted is a simple linear regression,
970 ignoring the groups. Next the model is extended to include a different constant (or intercept)

for each group, giving a set of parallel lines one for each group. Then, the final model has both a different constant and a different regression coefficient (or slope) for each group.

To avoid age-related differences in the case of in-house bred mice, multiple injection groups were pooled until we achieved the predetermined number of mice. The injection group was included as a factor in the statistical model specific for the read-out. For femur bending analysis, femur width was included into the model.

An unpaired t-test was used when comparing two groups. To compare multiple independent groups, we used one-way ANOVA with post-hoc Tukey's comparisons. Two-way ANOVA was performed to assess the significance between two factors. Measurements over time were analysed as repeated measurements analysis using the Restricted Maximum Likelihood (REML) approach, accounting for the correlation structure between observations, and assessing the significance of different factors, time, and interaction. Body weight data were adjusted for differences between baseline body weight.

Data availability

All raw data is available upon reasonable request with the exception of the human bone marrow single cell RNAseq data, which is being prepared for a second publication. If interested in this, please contact Stefan Dudli (Balgrist University Hospital). Bulk RNAseq data is uploaded on NCBI's Gene Expression Omnibus, accession code: GSE248918. This can be made available for the reviewers.

Computer code

Micro-CT analysis was performed on FiJi (ImageJ). The scripts are available upon request.

RNAseq/scRNAseq was analysed on R studio using freely available packages indicated in the methods section.

Methods references

49. Maschalidi, S. et al. Targeting SLC7A11 improves efferocytosis by dendritic cells and wound healing in diabetes. Nature 606, 776–784 (2022).

50. De Jager, W., Prakken, B. J., Bijlsma, J. W. J., Kuis, W. & Rijkers, G. T. Improved multiplex immunoassay performance in human plasma and synovial fluid following removal of interfering heterophilic antibodies. J Immunol Methods 300, 124–135 (2005).

51. Magno, R. & Maia, A. T. Gwasrapidd: An R package to query, download and wrangle GWAS catalog data. Bioinformatics 36, 649–650 (2020).

52. Lucas, D. et al. Chemotherapy-induced bone marrow nerve injury impairs hematopoietic regeneration. Nat Med 19, 695–703 (2013).

53. Gracey, E. et al. TYK2 inhibition reduces type 3 immunity and modifies disease progression in murine spondyloarthritis. Journal of Clinical Investigation 130, 1863–1878 (2020).

54. Masschaele, B. et al. HECTOR: A 240kV micro-CT setup optimized for research. in Journal of Physics: Conference Series vol. 463 (Institute of Physics Publishing, 2013).

55. Vlassenbroeck, J. et al. Software tools for quantification of X-ray microtomography at the UGCT. Nucl Instrum Methods Phys Res A 580, 442–445 (2007).

56. Gilis, E. et al. Deletion of Mucosa-Associated Lymphoid Tissue Lymphoma Translocation Protein 1 in Mouse T Cells Protects Against Development of

Autoimmune Arthritis but Leads to Spontaneous Osteoporosis. Arthritis and Rheumatology 71, 2005–2015 (2019).

57. Cambré, I. et al. Mechanical strain determines the site-specific localization of inflammation and tissue damage in arthritis. Nat Commun 9, (2018).

58. Buie, H. R., Campbell, G. M., Klinck, R. J., MacNeil, J. A. & Boyd, S. K. Automatic segmentation of cortical and trabecular compartments based on a dual threshold technique for in vivo micro-CT bone analysis. Bone 41, 505–515 (2007).

59. Kim, D., Langmead, B. & Salzberg, S. L. HISAT: A fast spliced aligner with low memory requirements. Nat Methods 12, 357–360 (2015).

60. Liao, Y., Smyth, G. K. & Shi, W. FeatureCounts: An efficient general purpose program for assigning sequence reads to genomic features. Bioinformatics 30, 923–930 (2014).

61. Love, M. I., Huber, W. & Anders, S. Moderated estimation of fold change and dispersion for RNA-seq data with DESeq2. Genome Biol 15, (2014).

62. Zhu, A., Ibrahim, J. G. & Love, M. I. Heavy-Tailed prior distributions for sequence count data: Removing the noise and preserving large differences. Bioinformatics 35, 2084–2092 (2019).

63. Yu, G., Wang, L. G., Han, Y. & He, Q. Y. ClusterProfiler: An R package for comparing biological themes among gene clusters. OMICS 16, 284–287 (2012).

64. Patel, C. et al. A New Method of Bone Stromal Cell Characterization by Flow Cytometry. Curr Protoc 2, (2022).

65. Zhu, J., Siclari, V. A. & Qin, L. Isolating endosteal mesenchymal progenitors from rodent long bones. Methods in Molecular Biology 1226, 19–29 (2015).

66. Coll, A. P. et al. GDF15 mediates the effects of metformin on body weight and energy balance. Nature 578, 444–448 (2020).

EXTENDED FIGURES AND FIGURE LEGENDS

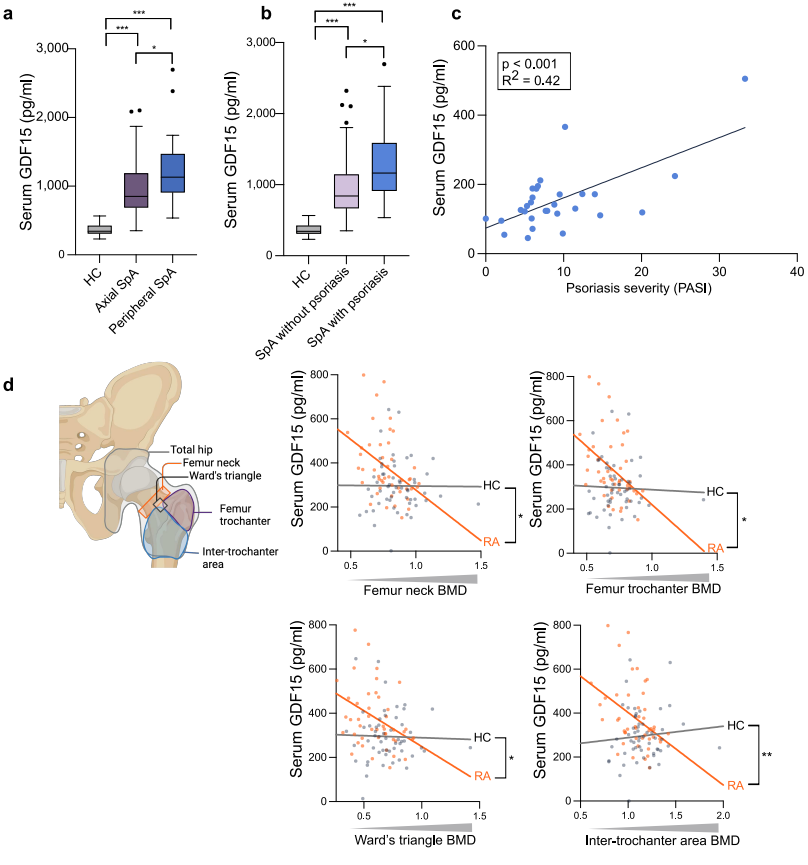
a
b
c
d
Serum GDF15 (pg/ml)
HC
Axial SpA
Peripheral SpA
SpA without psoriasis
SpA with psoriasis
p < 0.001
R2 = 0.42
Psoriasis severity (PASI)
Total hip
Femur neck
Ward's triangle
Femur trochanter
Inter-trochanter area
RA
Femur neck BMD
Femur trochanter BMD
Ward's triangle BMD
Inter-trochanter area BMD

Extended Data Fig. 1. Increased GDF15 levels in arthritis associates with low bone density **a,** Luminex was used to measure GDF15 in serum from HC (heathy controls, n = 19) and SpA (spondyloarthritis) patients, subdivided based on the presence of arthritis in axial (n = 71) or peripheral joints (n = 17). **b,** SpA patients were subdivided based on the presence (n = 16) or absence (n=95) of skin or nail psoriasis. Data are represented by Tukey box and whiskers plots. A one-way ANOVA was used to test for differences between patient means, followed by a post-hoc Tukey test. **c,** Simple linear regression was used to generate a regression line between serum GDF15 levels, determined by ELISA, and skin inflammation severity assessed using the Psoriasis Area and Severity Index (PASI) (n = 29). **d,** Serum GDF15 was measured by ELISA and bone mineral density (BMD) assessed by DEXA scan in RA patients (n = 46) and HC (n = 54). Simple linear regression with groups was used to generate regression lines between serum GDF15 and femur neck BMD, inter-trochanter BMD, femur trochanter BMD and Ward's triangle BMD, as indicated in the cartoon. The p-value refers to the significance of the difference in regression coefficients between patient groups HC and RA. Detailed information on statistics used can be found in Supplementary Table 1. Each datapoint represents one patient. For all datasets, serum GDF15 concentrations were adjusted for age. Significances are indicated as: * $p < 0.05$, ** $p < 0.01$, *** $p < 0.001$.

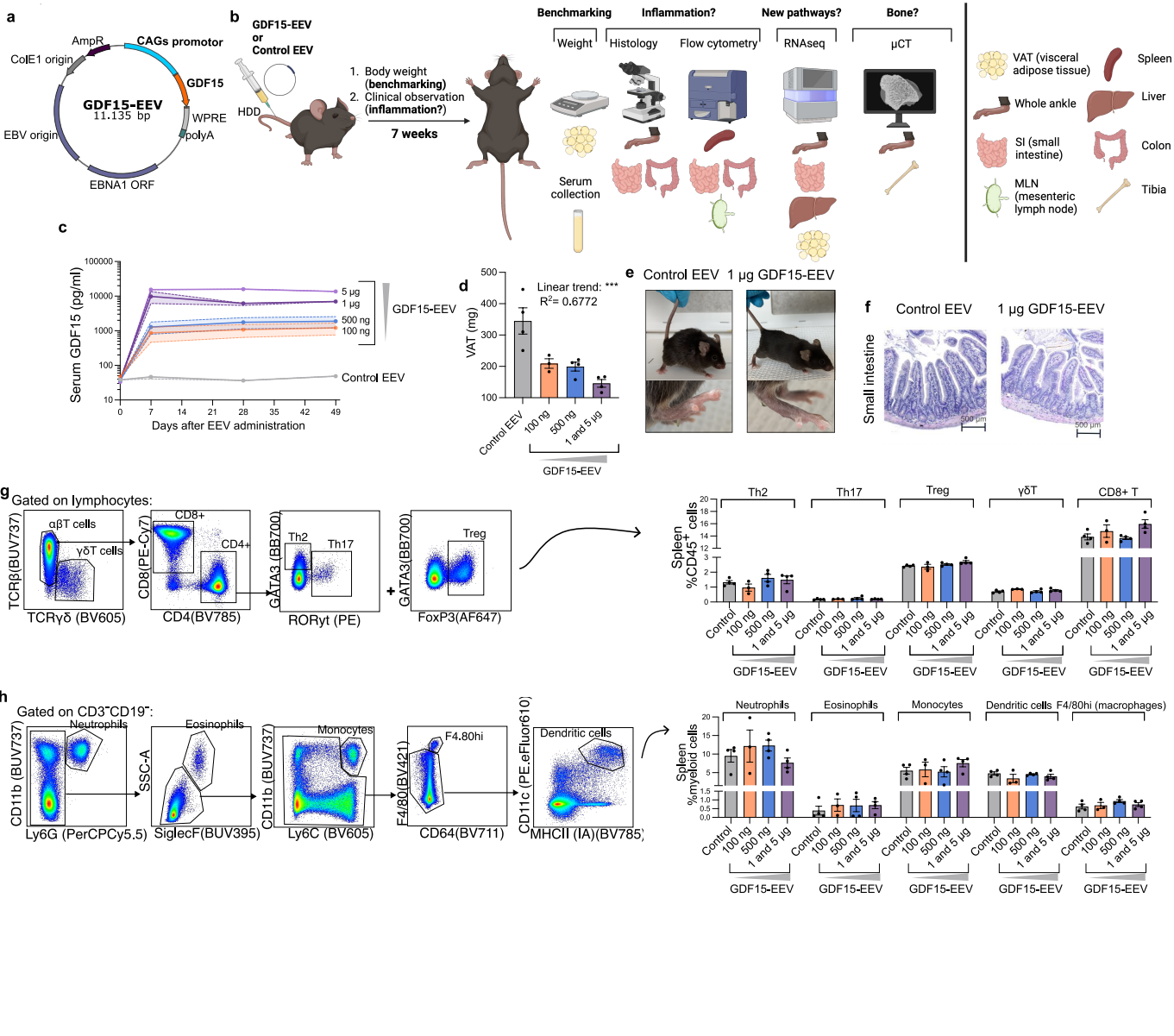
a
AmpR
CAGs promotor
ColE1 origin
GDF15
GDF15-EEV
11.135 bp
WPRE
polyA
EBV origin
EBNA1 ORF
b
GDF15-EEV
or
Control EEV
HDD
1. Body weight
(benchmarking)
2. Clinical observation
(inflammation?)
7 weeks
Benchmarking
Inflammation?
New pathways?
Bone?
Weight
Histology
Flow cytometry
RNAseq
µCT
Serum
collection
VAT (visceral
adipose tissue)
Spleen
Whole ankle
Liver
SI (small
intestine)
Colon
MLN
(mesenteric
lymph node)
Tibia
c
Serum GDF15 (pg/ml)
Days after EEV administration
5 µg
1 µg
500 ng
100 ng
GDF15-EEV
Control EEV
d
VAT (mg)
Linear trend: ***
R²= 0.6772
Control EEV
100 ng
500 ng
1 and 5 µg
GDF15-EEV
e
Control EEV
1 µg GDF15-EEV
f
Control EEV
1 µg GDF15-EEV
Small intestine
500 µm
g
Gated on lymphocytes:
αβT cells
γδT cells
TCRβ(BUV737)
TCRγδ (BV605)
CD8+
CD4+
CD8(PE-Cy7)
CD4(BV785)
Th2
Th17
GATA3 (BB700)
RORγt (PE)
Treg
FoxP3(AF647)
Th2
Th17
Treg
γδT
CD8+ T
Spleen
%CD45+ cells
Control
100 ng
500 ng
1 and 5 µg
GDF15-EEV
h
Gated on CD3⁻CD19⁻:
Neutrophils
Eosinophils
Monocytes
F4.80hi
Dendritic cells
CD11b (BUV737)
Ly6G (PerCPCy5.5)
SSC-A
SiglecF(BUV395)
Ly6C (BV605)
F4/80(BV421)
CD64(BV711)
CD11c (PE.eFluor610)
MHCII (IA)(BV785)
Neutrophils
Eosinophils
Monocytes
Dendritic cells
F4/80hi (macrophages)
Spleen
%myeloid cells

Extended Data Fig. 2. GDF15 does not induces tissue inflammation

a, Schematic of the GDF15 Enhanced Episomal Vector (GDF15-EEV). The same vector lacking the GDF15 sequence was used as control, named "Control EEV".

b, Schematic overview of the GDF15-Enhanced Episomal Vector (EEV) dose-response experiment. Increasing doses of GDF15-EEV or control EEV were injected using HDD (hydrodynamic) tail vein injection. The mice were weighed and clinically monitored for signs of inflammation and pain at least three times per week for seven weeks. Upon sacrifice, tissues were collected for processing as indicated in the schematic. **c,** Mouse GDF15 serum levels determined using ELISA. **d,** Visceral adipose tissue (VAT) weight upon sacrifice. A one-way ANOVA was used to test for differences in VAT between the doses, followed by post-hoc test for trend. **e,** Mice with control EEV or 1 μg GDF15-EEV display no visual signs of pain, dermatitis or arthritis. **f,** Representative H&E-stained microscopy images of small intestine. **g,** Gating strategy showing live, single, $CD45^+$ cells and cell frequencies for lymphoid cells in spleen. **h,** Gating strategy showing live, single, $CD3^-CD19^-$ cells and cell frequencies for myeloid cells in spleen.

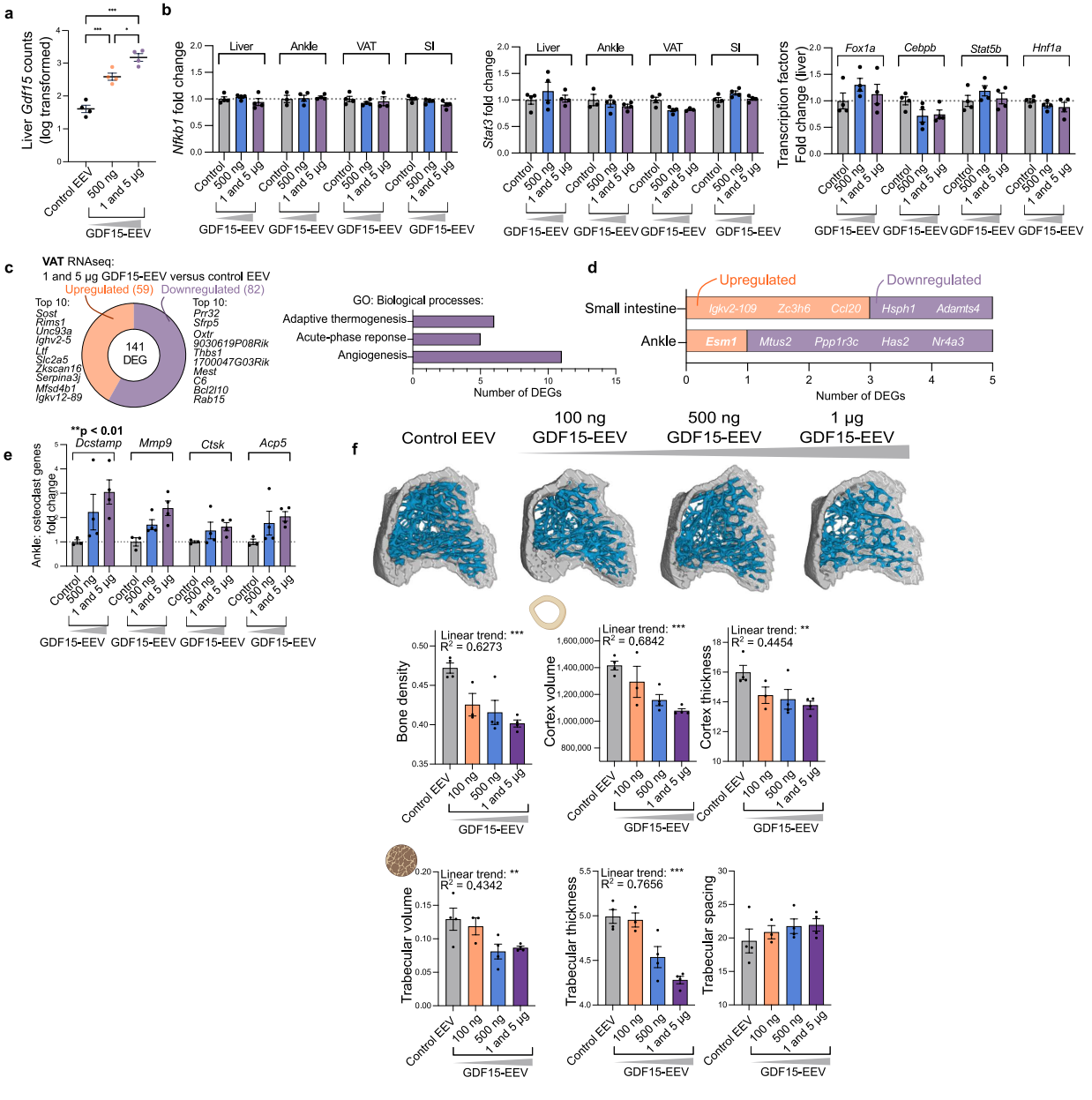
a
Liver Gdf15 counts (log transformed)
Control EEV
500 ng
1 and 5 µg
GDF15-EEV
b
Nfkb1 fold change
Stat3 fold change
Transcription factors Fold change (liver)
Liver
Ankle
VAT
SI
Fox1a
Cebpb
Stat5b
Hnf1a
Control
500 ng
1 and 5 µg
GDF15-EEV
c
VAT RNAseq:
1 and 5 µg GDF15-EEV versus control EEV
Upregulated (59)
Downregulated (82)
Top 10:
Sost
Rims1
Unc93a
Ighv2-5
Ltf
Slc2a5
Zkscan16
Serpina3j
Mfsd4b1
Igkv12-89
141 DEG
Top 10:
Prr32
Sfrp5
Oxtr
9030619P08Rik
Thbs1
1700047G03Rik
Mest
C6
Bcl2l10
Rab15
GO: Biological processes:
Adaptive thermogenesis
Acute-phase reponse
Angiogenesis
Number of DEGs
d
Upregulated
Downregulated
Small intestine
Igkv2-109
Zc3h6
Ccl20
Hsph1
Adamts4
Ankle
Esm1
Mtus2
Ppp1r3c
Has2
Nr4a3
Number of DEGs
e
**p < 0.01
Dcstamp
Mmp9
Ctsk
Acp5
Ankle: osteoclast genes fold change
Control
500 ng
1 and 5 µg
GDF15-EEV
f
Control EEV
100 ng GDF15-EEV
500 ng GDF15-EEV
1 µg GDF15-EEV
Bone density
Linear trend: ***
R² = 0.6273
Cortex volume
Linear trend: ***
R² = 0.6842
Cortex thickness
Linear trend: **
R² = 0.4454
Trabecular volume
Linear trend: **
R² = 0.4342
Trabecular thickness
Linear trend: ***
R² = 0.7656
Trabecular spacing
Control EEV
100 ng
500 ng
1 and 5 µg
GDF15-EEV

Extended Data Fig. 3. GDF15 induces dose-dependent bone loss

a, Liver *Gdf15* counts determined by bulk RNAseq, relative to control EEV. A one-way ANOVA was used to test for differences in gene expression between the doses, followed by a post-hoc Tukey's multiple comparison test. **b,** Left, *Nfkb1* and *Stat3* counts determined by bulk RNAseq in liver, ankle, VAT (visceral adipose tissue) and SI (small intestine), relative to control EEV. Right, inflammation-associated transcription factors in the liver determined by bulk RNAseq, relative to control EEV. **c,** Bulk RNAseq of VAT from control EEV versus 1 and 5µg GDF15-EEV treated mice. Total number of differentially expressed genes (DEGs) (log_2 fold change > 1.0 and < 1.0, adjusted p value < 0.05), and the top 10 up- and downregulated DEGs listed. Pathway analysis using GO (Gene Ontology) terms showing the biological processes ($p < 0.001$) to which the up- or downregulated DEGs contribute. **d,** Bulk RNAseq on SI and ankle (including skin, muscle and tendon) of control EEV versus 1/5 µg GDF15-EEV treated mice. Total number of differentially expressed genes (DEG) (log_2 fold change > 1.0 and < 1.0, adjusted p value < 0.05). **e,** In ankle; For each gene, counts normalized to control of genes displayed. A one-way ANOVA was used to test for the effect of EEV. **f,** Representative images of µCT of tibia shown, bone cortex in grey and trabeculae in blue. The indicated bone parameters were quantified. Bone density is the bone volume divided by total volume. Trabeculae volume is normalized to the total inside volume. A one-way ANOVA was used to test for differences between the four doses, followed by post-hoc test for trend. Data are represented as mean ± SEM, dots represent the individual mice. n.s. = not significant, * $p < 0.05$, ** $p < 0.01$, *** $p < 0.001$.

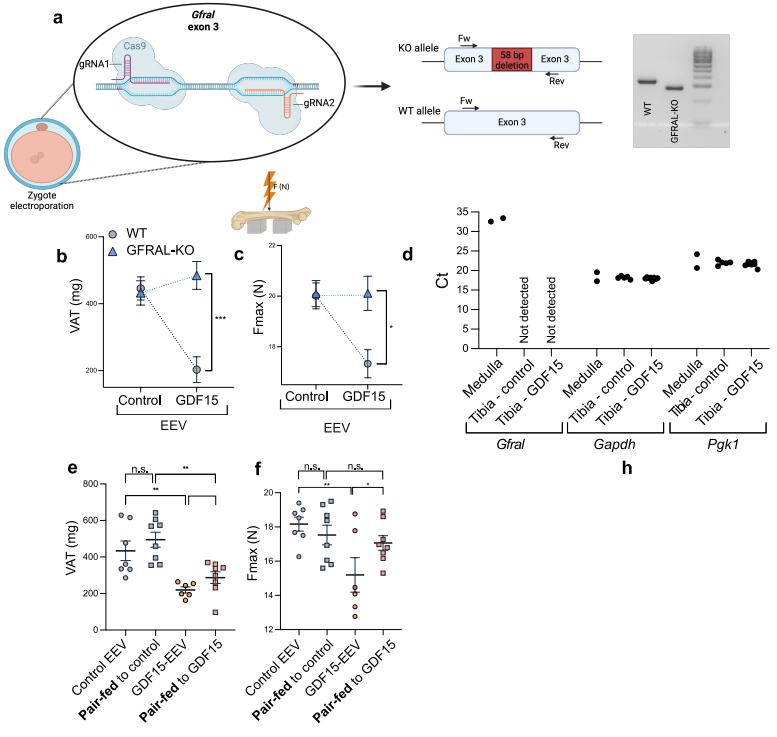
a
Gfral
exon 3
Cas9
gRNA1
gRNA2
Zygote
electroporation
KO allele
Fw
Exon 3
58 bp
deletion
Exon 3
Rev
WT allele
Fw
Exon 3
Rev
WT
GFRAL-KO
F (N)
b
WT
GFRAL-KO
VAT (mg)
Control
GDF15
EEV
c
Fmax (N)
Control
GDF15
EEV
d
Ct
Not detected
Not detected
Medulla
Tibia - control
Tibia - GDF15
Medulla
Tibia - control
Tibia - GDF15
Medulla
Tibia - control
Tibia - GDF15
Gfral
Gapdh
Pgk1
h
e
VAT (mg)
n.s.
Control EEV
Pair-fed to control
GDF15-EEV
Pair-fed to GDF15
f
Fmax (N)
n.s.
n.s.
Control EEV
Pair-fed to control
GDF15-EEV
Pair-fed to GDF15

Extended data Fig. 4. GDF15-induced bone loss is GFRAL-dependent, but independent from weight loss

a, CRISPR/Cas9 strategy to create GFRAL-KO mice. Using two gRNAs, 58 bp were deleted in exon 3 of the *Gfral* gene causing non-sense mediated decay. Right, gel electrophoresis of a GFRAL-KO mouse and a WT littermate. **b,** VAT (Visceral Adipose Tissue) weight of GFRAL-KO mice and WT littermates injected with GDF15-EEV or control EEV. **c,** Femoral strength assessed by three-point bending test. The Fmax (maximum force) is the load right before the bone fractures. A two-way ANOVA was used to test for interactions between Genotype (KO or WT) and EEV (GDF15 or control). **d,** qPCR performed on medulla (hindbrain) of WT mice and tibia of mice treated with control or GDF15-EEV. Ct values of the gene of interest *Gfral* and reference genes *Gapdh* and *Pgk1* are shown. Each datapoint represents an individual mouse. **e,** VAT (Visceral Adipose Tissue) weight of the pair-feeding experiment. **f,** Femoral strength assessed by three-point bending test. A one-way ANOVA was used to test for differences between the four groups, followed by post-hoc Šídák's multiple comparisons test. Results are represented as mean ± SEM. Dots represent the individual mice. Significance of the pairwise comparisons are indicated as: * $p < 0.05$, ** $p < 0.01$, *** $p < 0.001$.

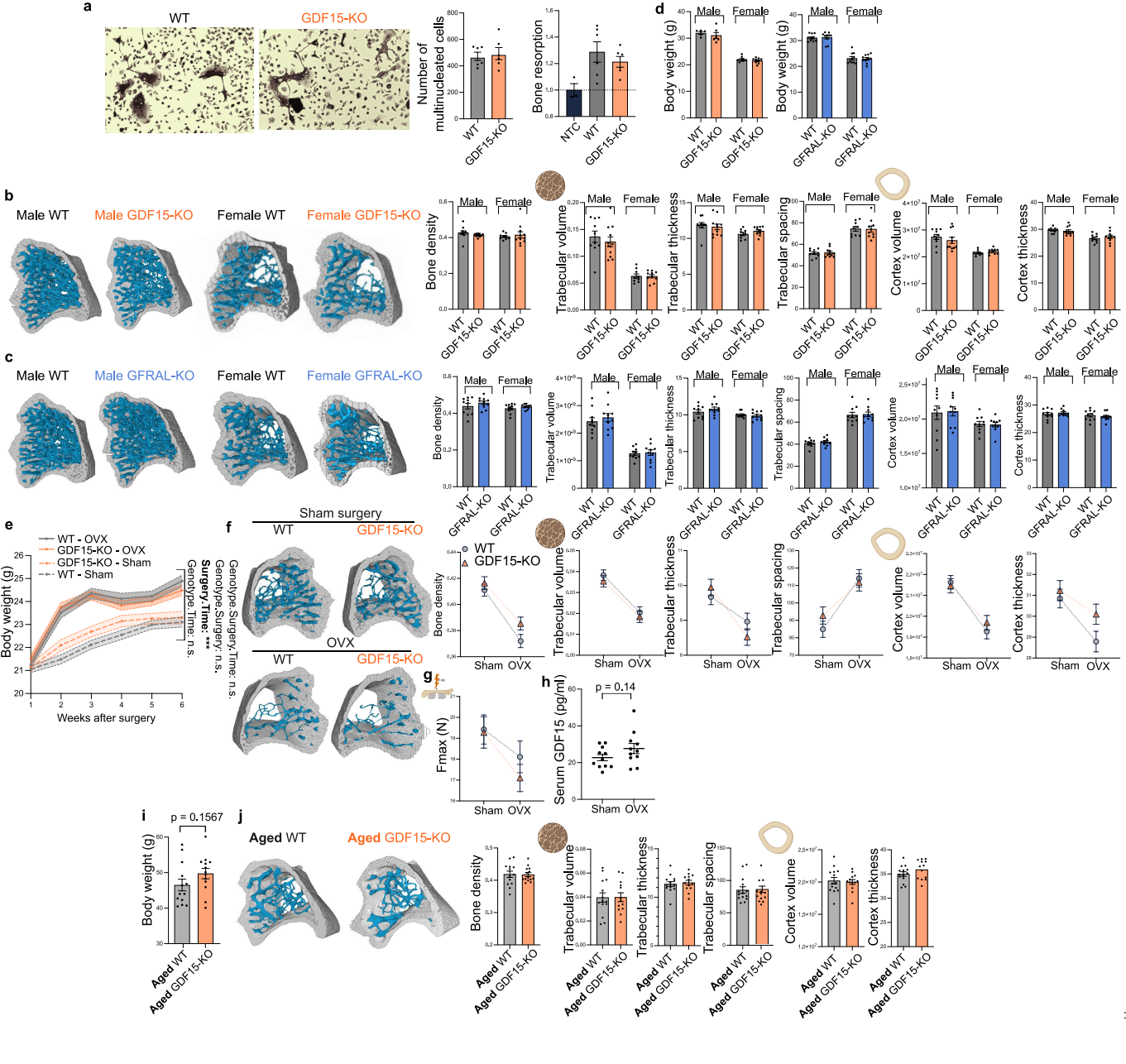
a
WT
GDF15-KO
Number of multinucleated cells
Bone resorption
NTC
WT
GDF15-KO
d
Male
Female
Body weight (g)
WT
GDF15-KO
GFRAL-KO
b
Male WT
Male GDF15-KO
Female WT
Female GDF15-KO
Bone density
Trabecular volume
Trabecular thickness
Trabecular spacing
Cortex volume
Cortex thickness
c
Male GFRAL-KO
Female GFRAL-KO
e
WT - OVX
GDF15-KO - OVX
GDF15-KO - Sham
WT - Sham
Body weight (g)
Weeks after surgery
Genotype.Time: n.s.
Surgery.Time: **
Genotype.Surgery.Time: n.s.
Genotype.Surgery: n.s.
f
Sham surgery
OVX
WT
GDF15-KO
g
Fmax (N)
Sham
OVX
h
p = 0.14
Serum GDF15 (pg/ml)
i
p = 0.1567
Body weight (g)
Aged WT
Aged GDF15-KO
j
Aged WT
Aged GDF15-KO

Extended Data Fig. 5. GDF15 is not required for steady-state and non-inflammatory bone homeostasis

a, Bone marrow was isolated from GDF15-KO mice and WT littermates and cultured *in vitro* with RANKL and M-CSF to differentiate into osteoclasts over 5 days (n = 6). Left, representative images of multinucleated osteoclasts. Right, number of multinucleated cells counted and quantitative analysis of bone resorption, as measured by fluorescence released by cells derived from GDF15-KO mice and WT littermates. NTC (negative control) are bone marrow cells stimulated with M-CSF, but not RANKL. An unpaired t-test was used to test for differences between GDF15-KO and WT. **b and c,** Representative μCT images of tibia of GDF15-KO (b) and GFRAL-KO (c) mice versus WT littermates, aged 14 weeks. **d,** Body weight at 14-weeks of age. **e,** GDF15-KO mice and WT littermates underwent ovariectomy (OVX) or sham surgery. A repeated measurements analysis was performed to assess overall changes over time in body weight between the four groups, represented by the interaction between genotype (KO or WT), surgery (OVX or Sham) and time. Body weights were adjusted for differences in baseline body weight. **f,** Representative μCT images of tibia shown. The indicated bone parameters were quantified. **g,** Femoral strength was assessed using a three-point bending assay. A two-way ANOVA was used to test for interactions between genotype (KO or WT) and surgery (OVX or Sham). **h,** Serum GDF15 levels determined by ELISA tested for differences between sham or OVX surgery in WT mice. **i,** Body weight of untreated, aged (15-month-old) male GDF15-KO and WT littermate mice (n = 13). An unpaired t-test was used to test the difference between the groups. **j,** Representative μCT images of tibia shown. The indicated bone parameters were quantified. Data are represented as mean ± SEM, dots represent the individual mice.

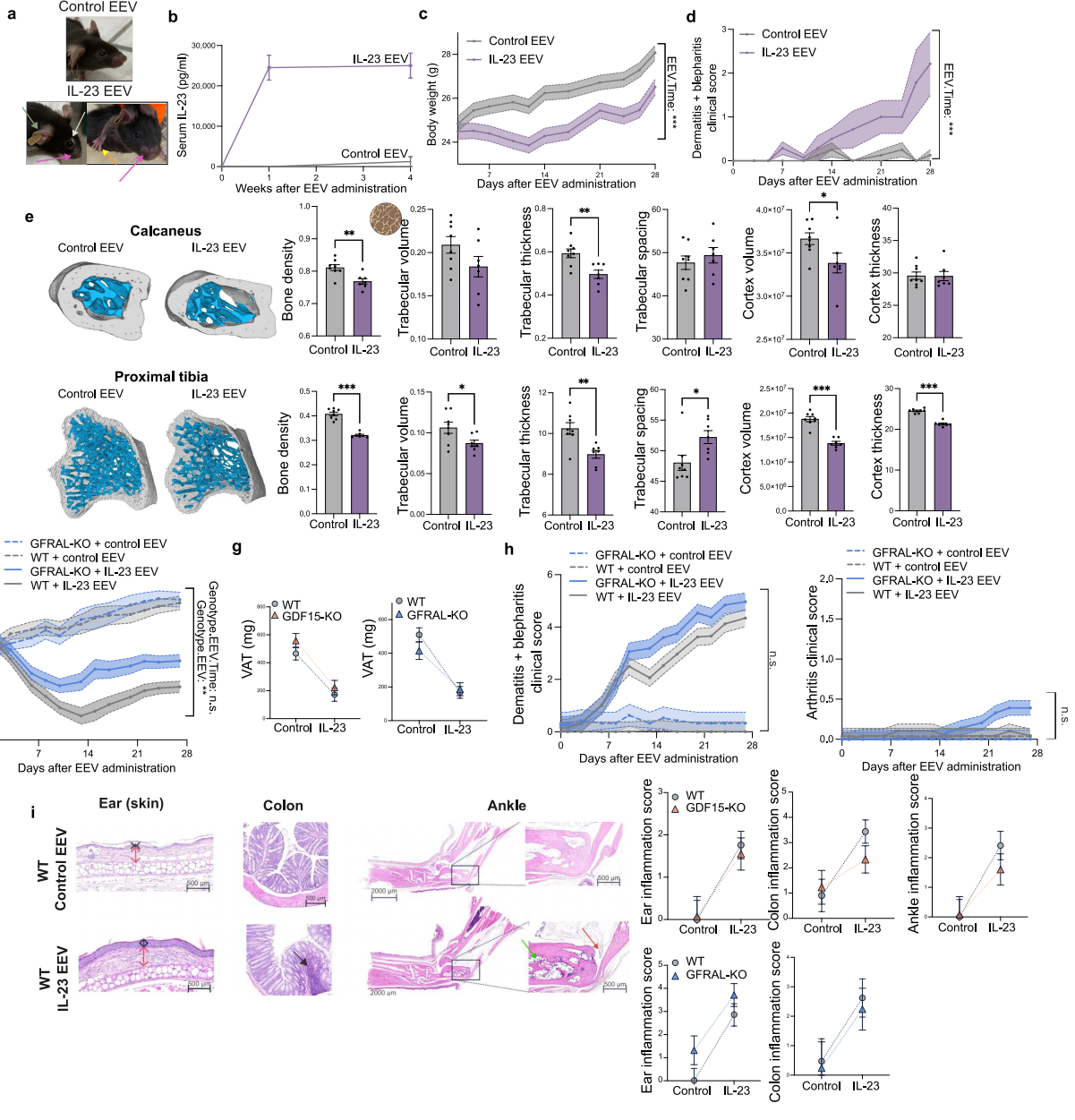
a
Control EEV
IL-23 EEV
b
Serum IL-23 (pg/ml)
IL-23 EEV
Control EEV
Weeks after EEV administration
c
Control EEV
IL-23 EEV
Body weight (g)
EEV.Time: ***
Days after EEV administration
d
Control EEV
IL-23 EEV
Dermatitis + blepharitis clinical score
EEV.Time: ***
Days after EEV administration
e
Calcaneus
Control EEV
IL-23 EEV
Bone density
Trabecular volume
Trabecular thickness
Trabecular spacing
Cortex volume
Cortex thickness
Control
IL-23
Proximal tibia
Control EEV
IL-23 EEV
Bone density
Trabecular volume
Trabecular thickness
Trabecular spacing
Cortex volume
Cortex thickness
Control
IL-23
f
GFRAL-KO + control EEV
WT + control EEV
GFRAL-KO + IL-23 EEV
WT + IL-23 EEV
Body weight (g)
Genotype.EEV.Time: n.s.
Genotype.EEV: **
Days after EEV administration
g
WT
GDF15-KO
VAT (mg)
Control
IL-23
WT
GFRAL-KO
VAT (mg)
Control
IL-23
h
GFRAL-KO + control EEV
WT + control EEV
GFRAL-KO + IL-23 EEV
WT + IL-23 EEV
Dermatitis + blepharitis clinical score
n.s.
Days after EEV administration
GFRAL-KO + control EEV
WT + control EEV
GFRAL-KO + IL-23 EEV
WT + IL-23 EEV
Arthritis clinical score
n.s.
Days after EEV administration
i
Ear (skin)
Colon
Ankle
WT
Control EEV
WT
IL-23 EEV
500 µm
2000 µm
WT
GDF15-KO
Ear inflammation score
Colon inflammation score
Ankle inflammation score
Control
IL-23
WT
GFRAL-KO
Ear inflammation score
Colon inflammation score
Control
IL-23

Extended Data Fig. 6. The GDF15-GFRAL axis mediates IL-23 induced weight loss, but not inflammation severity

a, Representative images of clinical manifestations of IL-23 EEV administration in WT mice. White arrow shows blepharitis; pink and green arrow shows dermatitis at the snout and ear respectively. Yellow arrow shows distal interphalangeal joint swelling. **b,** C57Bl/6J mice were injected with either IL-23 EEV or control EEV. Serum IL-23 levels were determined using ELISA. **c, d,** A repeated measurements analysis was performed to assess overall changes over time in body weight (c) or clinical scores (d) between the two EEV groups IL-23 or control, represented by the interaction between EEV and time. Body weights were adjusted for differences in baseline body weight. **e,** Representative μCT images of calcaneus and tibia shown. The indicated bone parameters were quantified. An unpaired t-test was used to test for difference between the treatment groups. Dots represent the individual mice. **f,** GFRAL-KO mice and WT littermates were administered either IL-23 EEV or control EEV (control EEV groups: n = 5-6, IL-23 EEV groups: n = 8-9) and weighed three times per week. A repeated measurements analysis was performed to assess overall changes over time between the groups, represented by the interaction between the Genotype (KO or WT) and EEV (IL-23 or control) and time. Body weights were adjusted for differences in baseline body weight. **g,** VAT (Visceral Adipose Tissue) weight after IL-23 overexpression upon sacrifice. **h,** Clinical scores for psoriasis-like dermatitis and blepharitis and arthritis. A repeated measurements analysis was performed to assess overall changes over time between the groups. **i,** Representative H&E-stained images and statistical analysis of histopathology. Ear: black arrow indicates epidermal thickness; red arrow indicates dermal thickness. Colon: black arrow shows immune cell infiltration. Ankle: green arrow indicates bone marrow oedema in calcaneus. Orange arrow indicates infiltration in the synovial-enthesial complex.

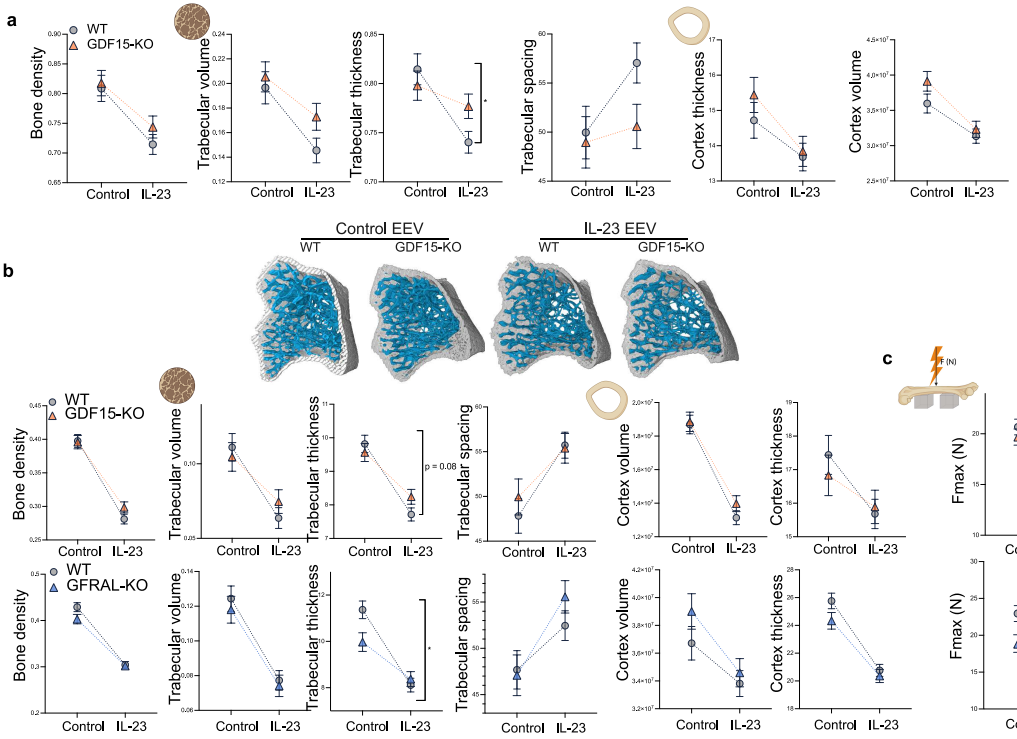
a
WT
GDF15-KO
Bone density
Trabecular volume
Trabecular thickness
Trabecular spacing
Cortex thickness
Cortex volume
Control
IL-23
b
Control EEV
IL-23 EEV
WT
GDF15-KO
GFRAL-KO
p = 0.08
c
F (N)
Fmax (N)

Extended Data Fig. 7. The GDF15-GFRAL axis mediates trabecular bone loss in the IL-23 EEV model

a, For IL-23 EEV treated GDF15-KO mice, the indicated calcaneus bone parameters were quantified. **b,** Representative μCT images of tibia shown, with the bone cortex in grey and trabeculae in blue. The indicated bone parameters were quantified. A two-way ANOVA was used to test for interactions between Genotype (KO or WT) and EEV (IL-23 or control). **c,** Femoral strength assessed by three-point bending test. Results are represented as mean ± SEM. Significances of the interactions are indicated as: * $p < 0.05$.

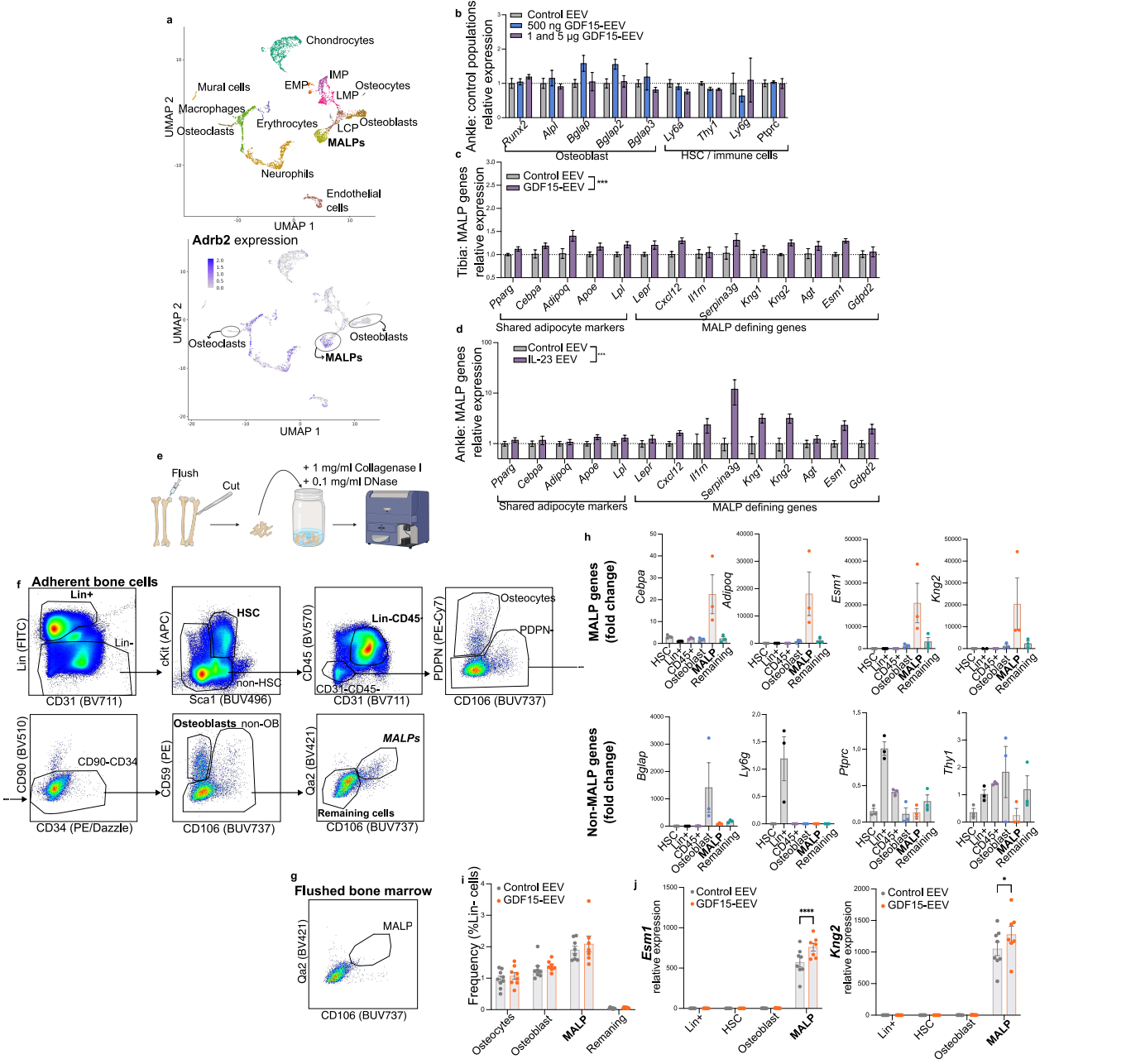
a
Chondrocytes
IMP
EMP
Osteocytes
LMP
Mural cells
Macrophages
Erythrocytes
LCP
Osteoblasts
Osteoclasts
MALPs
Neurophils
Endothelial cells
UMAP 2
UMAP 1
Adrb2 expression
Osteoclasts
Osteoblasts
MALPs
b
Control EEV
500 ng GDF15-EEV
1 and 5 µg GDF15-EEV
Ankle: control populations relative expression
Runx2
Alpl
Bglap
Bglap2
Bglap3
Ly6a
Thy1
Ly6g
Ptprc
Osteoblast
HSC / immune cells
c
Control EEV
GDF15-EEV
***
Tibia: MALP genes relative expression
Pparg
Cebpa
Adipoq
Apoe
Lpl
Lepr
Cxcl12
Il1rn
Serpina3g
Krg1
Krg2
Agt
Esm1
Gdpd2
Shared adipocyte markers
MALP defining genes
d
Control EEV
IL-23 EEV
***
Ankle: MALP genes relative expression
e
Flush
Cut
+ 1 mg/ml Collagenase I
+ 0.1 mg/ml DNase
f
Adherent bone cells
Lin+
Lin-
Lin (FITC)
CD31 (BV711)
cKit (APC)
Sca1 (BUV496)
HSC
non-HSC
CD45 (BV570)
Lin-CD45-
CD31-CD45-
PDPN (PE-Cy7)
Osteocytes
PDPN+
CD106 (BUV737)
CD90 (BV510)
CD90-CD34
CD34 (PE/Dazzle)
CD59 (PE)
Osteoblasts non-OB
Qa2 (BV421)
MALPs
Remaining cells
CD106 (BUV737)
g
Flushed bone marrow
MALP
Qa2 (BV421)
CD106 (BUV737)
h
MALP genes (fold change)
Cebpa
Adipoq
Esm1
Krg2
Non-MALP genes (fold change)
Bglap
Ly6g
Ptprc
Thy1
HSC
Lin+
CD45+
Osteoblast
MALP
Remaining
i
Control EEV
GDF15-EEV
Frequency (%Lin- cells)
Osteocytes
Osteoblast
MALP
Remaining
j
Control EEV
GDF15-EEV
Esm1 relative expression
Kng2 relative expression
****
Lin+
HSC
Osteoblast
MALP

Extended Data Fig. 8. GDF15 activates MALPs to produce RANKL and M-CSF

a, The single-cell dataset (scRNAseq) from 3-month-old mice from Zhong et al. annotated by clusters according to their published paper and β_2-adrenergic receptor (*Adrb2*) expression. EMP = Early Mesenchymal Progenitor; IMP = Intermediate Mesenchymal Progenitor; LMP = Late Mesenchymal Progenitor; LCP = Lineage Committed Progenitor, MALP = Marrow Adipogenic Lineage Precursor. **b,** Counts of osteoblast, immune cell and HSC (hematopoietic stem cell) associated genes as determined in joint RNAseq of mice treated with GDF15-EEV. Each gene is normalized to control EEV. **c,** Relative gene expression in proximal tibia of mice treated with GDF15-EEV or control EEV determined by qPCR, normalized to reference genes *Gapdh* and *Pgk1* and relative to control EEV (n = 5-7). **d,** Relative gene expression on ankles from mice treated with IL-23 EEV or control EEV (n = 6). A One-way ANOVA was used to assess the effect of the EEV. **e,** Mouse MALP frequency and activation were assessed using FACS. A schematic of sample processing is shown. First, hind leg bones were cleaned, flushed and cut longitudinally and into small pieces. Bone pieces were digested with collagenase I and DNase for 60min at 37°C, after which cells were stained for FACS. **f,** Gating strategy to identify MALPs in adherent bone cells. Live, single cells are shown. Selected cell populations shown in bold were sorted to determine gene expression. **g,** MALPs are lacking in the non-adherent, flushed bone marrow. **h,** Gene expression in sorted adherent bone cells, normalized to reference gene *Gapdh* and relative to Lin+ cells. **i,** Adherent bone cells of mice treated with GDF15-EEV or control EEV analysed using flow cytometry. Frequency (% of Lin- cells) of the indicated cell types is shown. **j,** MALP-defining genes *Esm1* and *Kng2* expression relative to Lin^+ in sorted cells treated with GDF15-EEV or control EEV. A two-way ANOVA was used, followed by a post-hoc Tukey's multiple comparison test. Results are represented as mean ± SEM. Dots represent individual mice. Significance is indicated as: * $p < 0.05$, **** $p < 0.001$.

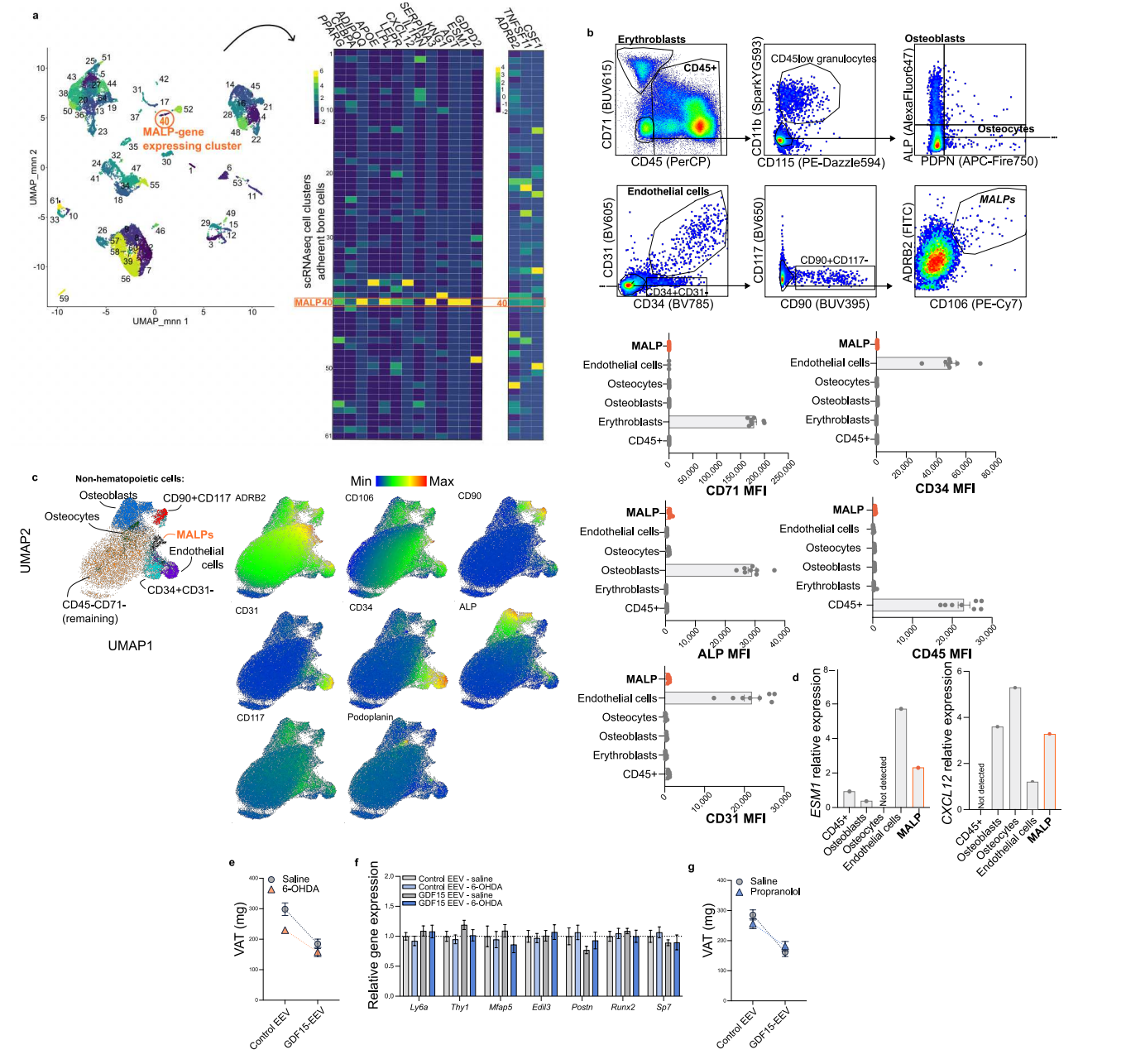
a
MALP-gene expressing cluster
UMAP_mnn 1
UMAP_mnn 2
scRNAseq cell clusters adherent bone cells
MALP40
b
Erythroblasts
CD45+
CD71 (BUV615)
CD45 (PerCP)
CD45low granulocytes
CD11b (SparkYG593)
CD115 (PE-Dazzle594)
Osteoblasts
Osteocytes
ALP (AlexaFluor647)
PDPN (APC-Fire750)
Endothelial cells
CD34+CD31+
CD31 (BV605)
CD34 (BV785)
CD90+CD117-
CD117 (BV650)
CD90 (BUV395)
MALPs
ADRB2 (FITC)
CD106 (PE-Cy7)
MALP
Endothelial cells
Osteocytes
Osteoblasts
Erythroblasts
CD45+
CD71 MFI
CD34 MFI
ALP MFI
CD45 MFI
CD31 MFI
c
Non-hematopoietic cells:
Osteoblasts
CD90+CD117
Osteocytes
MALPs
Endothelial cells
CD34+CD31-
CD45-CD71-
(remaining)
UMAP1
UMAP2
Min
Max
ADRB2
CD106
CD90
CD31
CD34
ALP
CD117
Podoplanin
d
ESM1 relative expression
CXCL12 relative expression
Not detected
CD45+
Osteoblasts
Osteocytes
Endothelial cells
MALP
e
Saline
6-OHDA
VAT (mg)
Control EEV
GDF15-EEV
f
Relative gene expression
Control EEV - saline
Control EEV - 6-OHDA
GDF15 EEV - saline
GDF15 EEV - 6-OHDA
Ly6a
Thy1
Mfap5
Edil3
Postn
Runx2
Sp7
g
Saline
Propranolol
VAT (mg)
Control EEV
GDF15-EEV

Extended Data Fig. 9. MALP cells are present in human bones

a, scRNAseq on digested human vertebral biopsies. Left, heatmap of the MALP gene signature by cell cluster. Right, heatmap showing expression of *RANKL, CSF1* and *ADRB2*. **b,** Gating strategy to identify MALPs in enzymatically digested human knee biopsies (n = 8). Gated on live, single cells. Selected cell populations shown in bold sorted to determine gene expression. MFI (Mean Fluorescence Intensity) of selected surface markers. Each datapoint represents one patient. **c,** UMAP projection of $CD45^-CD71^-CD115^-CD11b^-$ cells with cell populations overlayed and surface marker expression. **d,** MALPs and other major cell populations in the bone were sorted and gene expression was determined in two pooled human samples. Expression is normalized to reference gene *GAPDH.* **e,** Mice overexpressing GDF15 underwent chemical sympathectomy using 6-OHDA. VAT (Visceral Adipose Tissue) weight upon sacrifice is shown. **f,** Relative gene expression of the proximal tibia. The indicated genes are negative control genes, expressed by adherent bone cells, but not expressed by MALPs. Gene expression was normalized to reference genes *Gapdh* and *Pgk1* and relative to the "Control EEV – saline" group. **g,** Mice overexpressing GDF15 were treated with propranolol. VAT (Visceral Adipose Tissue) weight upon sacrifice is shown. Results are represented as mean ± SEM.

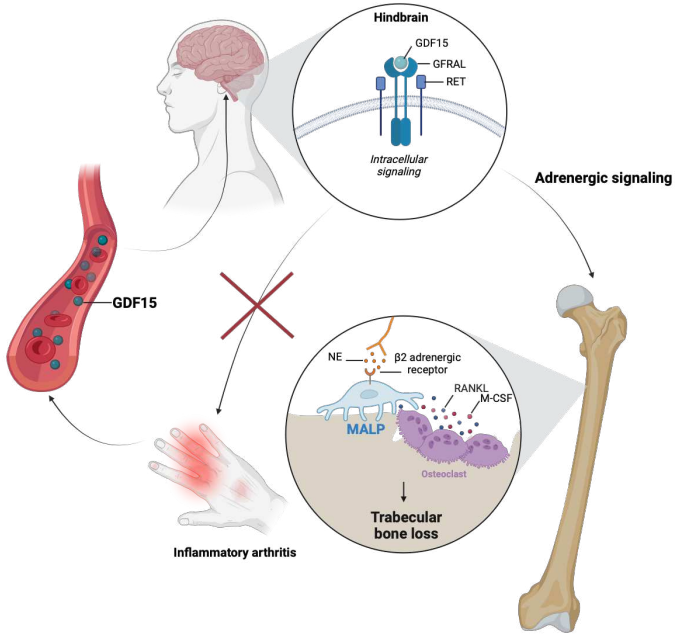
Hindbrain
GDF15
GFRAL
RET
Intracellular signaling
Adrenergic signaling
GDF15
NE
β2 adrenergic receptor
RANKL
M-CSF
MALP
Osteoclast
Trabecular bone loss
Inflammatory arthritis

Extended Data Fig. 10. Summary of the findings

Schematic of the overall conclusions.

Supplementary Files

This is a list of supplementary files associated with this preprint. Click to download.

- Supplementarymethods.docx
- Supplementarytables.docx